The Thesis Committee for Charles Jae Doolittle
Certifies that this is the approved version of the following thesis:

Near-Field Flow Structures and Transient Growth Due to Subcritical

Surface Roughness

APPROVED BY

SUPERVISING COMMITTEE:

Supervisor:

David Goldstein

Charles Tinney

Near-Field Flow Structures and Transient Growth Due to Subcritical Surface Roughness

by

Charles Jae Doolittle, B. Aero. Eng.

Thesis

Presented to the Faculty of the Graduate School of

The University of Texas at Austin

in Partial Fulfillment

of the Requirements

for the Degree of

Master of Science in Engineering

The University of Texas at Austin

May 2010

Dedication

This work is dedicated to my family, Chuck, Julie, and Justine Doolittle.

Acknowledgements

May 2010

Abstract

Near-Field Flow Structures and Transient Growth Due to Subcritical Surface Roughness

Charles Jae Doolittle, M. S. E.

The University of Texas at Austin, 2010

Supervisor: David Goldstein

An immersed boundary spectral method is used to simulate laminar boundary layer flow over a periodic array of cylindrical surface roughness elements. Direct comparisons are made with experiments by using a roughness-based Reynolds number Re_k of 216 and a diameter to spanwise spacing ratio d/λ of 1/3. Near-field differences between three similar studies are presented and addressed. The shear layer developed over the roughness element produces the downstream velocity deficit region while splitting of the vortex sheet shed the trailing edge forms its lateral modes. Additional geometrical configurations are simulated for comparisons with experimental results and future analysis by linear stability theory. Total disturbance energy E_{rms} is fairly consistent with experimental results while spanwise energy components vary significantly. Physical relaxation of the disturbance wake is found to remain a prominent issue for this simulation technique.

Table of Contents

NOMENCLATURE

d	= roughness element diameter
E	= integrated downstream disturbance energy
E_{rms}	= total disturbance energy
E_U, E_V	= percent error in Blasius profile, $100\times\left|(U-U_B)/U_\infty\right|$, $100\times\left|(V-V_B)/U_\infty\right|$
$E_{\lambda/m}$	= spanwise component of disturbance energy
F	= immersed boundary forcing function
k	= roughness element height
m	= spanwise wavelength number
$MIPV$	= magnitude of in-plane velocity, $\sqrt{V^2+W^2}$
N_x, N_y, N_z	= streamwise, wall normal, and spanwise number of grid points
PSD_m	= power spectral density of mode m
Re_k	= roughness height-based Reynolds number, $U(k)k/v$
Re_d	= roughness diameter-based Reynolds number, $U_\infty d/v$
Re_c	= code Reynolds number, $1/v$
Re_x	= streamwise distance-based Reynolds number, $U_\infty x/v$
S	= surface stagnation point
t	= time
U, V, W	= streamwise, wall normal, and spanwise velocity components
U_B, V_B	= streamwise and wall normal velocities of analytic Blasius boundary layer
$U(k)$	= streamwise velocity at roughness element height
U_∞	= user specified freestream streamwise velocity, 12.2m/s
U', V', W'	= disturbance velocity components, $U - U_B$
$\hat{U}_m$	= Fourier coefficient of the spanwise disturbance velocity signal
w	= buffer zone length
x, y, z	= streamwise, wall normal, and spanwise cartesian coordinates
x_{center}	= buffer zone center
x_k	= distance of roughness element from leading edge
β	= spanwise wavenumber
δ	= boundary layer scale, $\delta^*/1.7208$
δ_{99}	= boundary layer thickness based on 99% U_∞
δ^*	= displacement thickness, $\int_0^\infty \left(1-U/U_\infty\right)dy$
λ	= roughness element spanwise spacing, 19mm
η	= Blasius wall normal coordinate, y/δ
θ, φ	= integral and proportional immersed boundary parameters
v	= kinematic viscosity
$\omega_x, \omega_y, \omega_z$	= streamwise, wall normal, and spanwise vorticity

I. INTRODUCTION

Transition in flat plate boundary layers can be analytically described by linear stability theory under the assumption of infinitesimal, two-dimensional disturbances. In this context the boundary layer is found to be sensitive to exponentially growing Tollmien-Schlichting (T-S) waves. The eventual breakdown of T-S waves is noted as the primary mechanism of transition found in careful laboratory experiments.

Practical applications often cannot be described by linear theory as disturbances affecting the boundary layer (rough surfaces, freestream turbulence, vibrations, etc.) are commonly much more complex than those assumed by theory. In such instances minimal T-S wave growth occurs as other 'bypass' mechanisms drive the transition to turbulence. Some disturbances leading to bypass transition have been found to experience transient growth[1,2] in which disturbance kinetic energy grows algebraically even though instabilities are exponentially decaying. Distributed surface roughness has been shown to induce transient growth in flat plate boundary layers.[3,4]

Algebraic growth occurs when streamwise oriented vortices move high-speed flow of the upper boundary layer to lower regions and in turn 'lift-up' low-momentum flow to higher regimes.[2] These vortices act as steady disturbances that exponentially decay with downstream distance. Energy loss corresponding to vortex decay may be surpassed by the increase of disturbance energy associated with redistribution of momentum in the shear layer, the algebraic growth previously described.[5] If the disturbance energy growth reaches a critical level transition to turbulence will occur shortly downstream. Otherwise, these vortices can no longer effectively transfer fluid and the streamwise streaks associated with them exponentially decay, allowing the primary T-S transition process to take over.

A. Early Work

Transient growth theory initially explored the analysis of disturbances undergoing the maximum amount of transient growth within specific boundary layer conditions. These 'optimal' perturbations were presented by way of the linearized disturbance Navier-Stokes equations, the eigenmodes of which are nonorthogonal, creating coupled Orr-Sommerfield and Squire modes. Superposition of these exponentially decaying modes develops a transient period of kinetic energy growth.[6] Experiments by Reshotko and Leventhal[3] and White[4] displayed transient growth in subcritical flat plate flow past distributed roughness. Andersson et al.[7] simulated the maximum transient growth of optimal steady disturbances in a Blasius profile. This problem was solved analytically in the context of a parallel-flow, initial value problem which described the optimal disturbance as a steady streamwise oriented vortex that produced downstream streaks.[8]

Limitations of the initial transient growth theory appeared to stem from the lack of adequate representation of the near-field details of boundary layer flow over rough surfaces.[4] To correctly model realistic disturbances produced by surface roughness, the near-field flow structure may need to be determined computationally as experiments are generally limited by physical constraints.

Near-field details impact how surface roughness introduces disturbances into the boundary layer as well as how it initializes conditions for the growth of instabilities.[9] This receptivity to disturbances is well understood for modal cases, such as with T-S waves, wherein discrete disturbance modes are triggered by the particular environmental forcing.[10] However, within the context of transient growth, all disturbance modes contribute to energy growth. Receptivity, therefore, sets the initial disturbance amplitudes, algebraic growth rate, and location of largest growth through the distribution

of disturbance energy between decaying modes of the continuous spectrum of eigenmodes.[4]

B. Recent Efforts

In lieu of optimal disturbance theory's inability to accurately predict disturbance growth, a rigorous measure of receptivity was developed by Tumin.[11] Here decomposition of the biorthogonal eigenfunction system (BES) is applied to the perturbed boundary layer to generate amplitudes of the continuous spectrum modes. Unfortunately, application of this method requires all disturbance velocity components, limiting its use as V' and W' are often difficult to obtain experimentally.[4,12] Recently, this approach has been utilized with Direct Numerical Simulation (DNS) of flow about cylindrical roughness elements and furthered by reducing the number of flow parameters required for analysis, allowing for similar decomposition of experimental results.[13,14] The method has been shown effective in reconstructing the disturbance energy evolution downstream of the roughness elements from a single downstream two-dimensional slice of data (see Fig. 1).
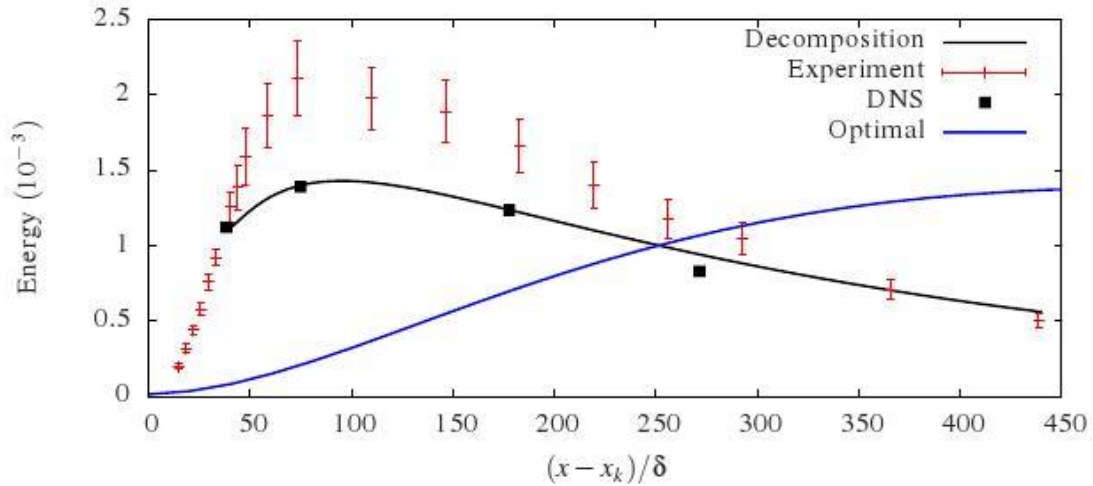

Fig. 1 Disturbance energy evolution of the λ/3 wavelength. Biorthogonal decomposition is performed on the furthest upstream DNS data set (black squares) and used to reconstruct the remainder of the flowfield (black line). Experimental results (red marks) do not match the decomposition due to discrepancies with DNS. The optimal disturbance energy profile (blue line) clearly does not capture physical results. Taken from Denissen et. al.[13]

3

Experiments performed at Case Western Reserve University by White[4] and White et al.[12] (WRE) found that the energy distribution of the continuous modes had a strong dependence on a number of roughness geometrical features, confirming the need again for a sophisticated receptivity model as an addition to optimal disturbance theory. To this end, experiments were carefully performed by Ergin and White[15] (EW) on a flat plate zero-pressure gradient flow over an array of cylindrical surface roughness elements evenly distributed in the spanwise direction by $\lambda = 3d$. Velocity measurements were acquired downstream of the elements via hotwire anemometry. The dependence on roughness height based Reynolds number Re_k was explored by testing two subcritical configurations (202 and 264) and one supercritical case (334). An advantage of the periodic array approach is the direct input of specific β which can be analyzed theoretically. DNS was concurrently applied to this setup by Rizzetta and Visbal[16] (RV) and found to be an excellent compliment to experimental work.

Stephani and Goldstein[17] (SG) further examined the configuration. They simulated the Re_k 202 and 334 experiments and found discrepancies in the 202 case when comparing with experiments of EW[15] and the DNS of RV.[16] Of primary issue was the near-field flow structure about the roughness elements. In the near-wake, velocity contours displayed 'bumps' in the flow deficit region centered downstream of the roughness element (see Fig. 2). Spanwise experimental resolution was questioned as DNS data could be superimposed onto the *experimental* mesh to produce nearly identical results as the experiments. Also, upstream vortex topology in the recirculation region differed between the RV and SG DNS sets, although the cause was not addressed.
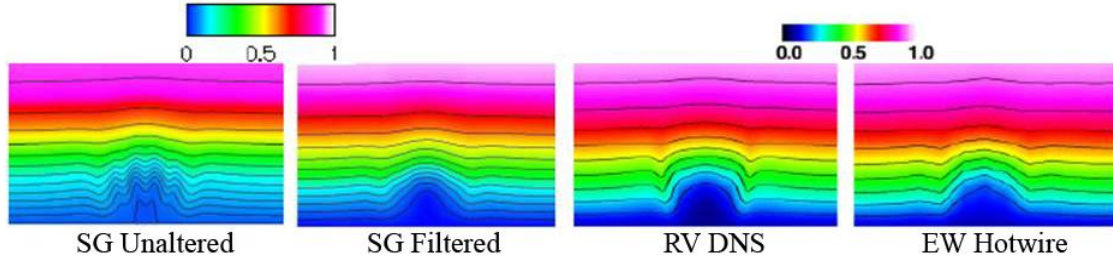
4

Fig. 2 Streamwise velocity contours approximately 3/2*d* downstream of roughness element. 'Bumps' found in DNS of SG were removed when data were interpolated onto a spanwise grid similar to that of the hotwire experiments of EW. Figure taken from SG.[17]

C. Flow Structures

The flow structure about these cylindrical surface roughness elements has features of both flow around cylindrical junctures and flow over two-dimensional sharp-edged surface obstacles. Characteristics of boundary layer flow over a two-dimensional sharp-edged surface obstacle include a large upwelling of fluid with a sharp increase of spanwise vorticity at the leading edge as well as a downstream recirculation region due to separation of the shear layer at the trailing edge.[18,19] Cylindrical juncture flow involves the formation of counter rotating vortex pairs stemming from the upstream recirculation region and a downstream region of reversed flow.[18,20] Interaction of these flow structures creates a complex environment in the roughness element near-field as visualized by Gregory and Walker.[21]

Details upstream of the elements, within roughly one cylinder diameter, may be suggested by juncture flow empirical results of Baker.[20] His experiments involved an extensive range of short cylinders mounted on a flat plate. A smoke filament was positioned upstream of the cylinders to visualize vortex topology and data were presented based upon configuration properties (see Fig. 3). Two, four, and six steady vortex topologies were found consisting of horseshoe and trailing vortex legs stemming from the

5

recirculation region and complimentary smaller counter rotating vortex cores closer to the plate surface.
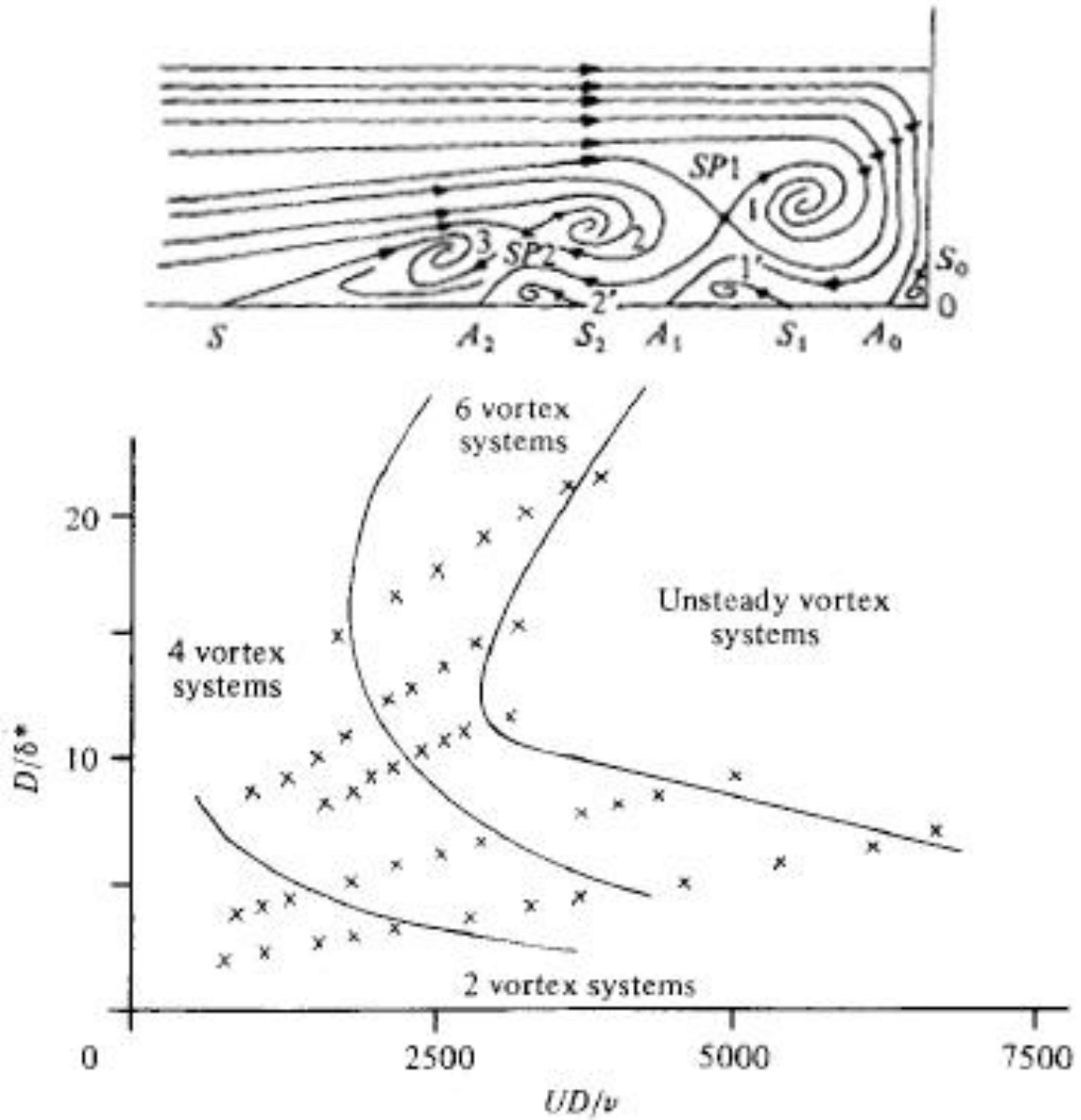

Fig. 3 Schematic of 6 vortex system upstream of a circular juncture (top) and variation of upstream vortex topology due to nondimensional parameters (bottom) developed by C. J. Baker[20] using smoke filament visualization.

6

Understanding the mechanisms involved with this type of transition is critical for real world applications. Aerodynamic vehicles commonly have rough surfaces capable of transitioning their own boundary layers and as such must operate at higher drag. A first step in delaying transition, and in turn reducing costs for many engineering applications, is the ability to accurately describe and predict transition. A framework for the development of transient growth theory has been summarized where analytic predictions can be made from computer simulations and verified by experiments.

D. Thesis Organization

This thesis is divided into eight chapters including the above introduction. Chapter II discusses the numeric method used for simulations. Chapter III intends to validate the use of an immersed boundary approach in a spectral DNS method as a viable option for simulating disturbance fields of distributed surface roughness. Chapter IV will attempt to resolve discrepancies presented by SG[17] so that a confident description of the local flow physics may be made. Details of these near-field flow structures and their subsequent interactions with the boundary layer will be addressed in Chapter V. Quantitative measures of transient growth will be presented in Chapter VI. Flow field temporal variation during the extent of the simulations will be addressed in Chapter VII along with predictions of the additional simulation time required to reach steady state. Finally, conclusions to be drawn from this study are discussed in Chapter VIII.

II. NUMERICAL METHOD

A. Spectral DNS

Current simulations utilize a channel flow spectral method similar to that of Kim et al.[22] coupled with an immersed boundary technique.[23] Simulations may be applied to laminar or turbulent flows over stationary or moving surfaces. Code verification has been performed on a variety of flow configurations.[24-26] The spectral approach involves modeling spatial derivatives of the incompressible Navier-Stokes equations with a Fourier series in the streamwise and spanwise directions and a Chebychev polynomial expansion in the wall normal direction. Streamwise and spanwise directions are therefore periodic. The streamwise periodicity may be removed to simulate a growing boundary layer. To avoid aliasing errors, the number of collocation points in both Fourier directions are increased by 3/2 times before transforming to physical space. Spatial resolution is varied in the Chebychev direction with a cosine grid, allowing for a large number of computational points to be clustered at either boundary. A semi-implicit time advancement scheme is used in which the viscous terms are solved with a Crank-Nicholson approach and nonlinear terms with an Adams-Bashforth method.[27] Our immersed boundary technique compliments spectral DNS because it allows for the use of fast transform methods while avoiding certain geometric constraints on the domain.

B. Immersed Boundaries

Virtual surfaces and immersed boundaries are created by introducing a local body force into the Navier-Stokes equations.[23] Velocities are specified at desired grid points and the forcing terms adjust to bring flow to the intended values. Forcing adaptation is controlled by an integral term based on a point's velocity history as well as a term using feedback of the current velocity. Gain parameters, θ and φ, manipulate these terms spatially within the forcing function,

$$F(x,t) = \theta \int\limits_{0}^{t} \left[U(x,t') - U_{des}(x,t') \right] dt' + \varphi \left[U(x,t) - U_{des}(x,t) \right], \tag{1}$$

where $U(x,t)$ is the current velocity vector at the point of interest and $U_{des}(x,t)$ is the user specified velocity vector. To aid in the development of 'smooth' surfaces, the forcing function is distributed to neighboring points in the periodic directions with a Gaussian profile. An additional parameter can be adjusted to vary the extent of this distribution. By limiting this spreading to the periodic directions, geometries can be created with sharp-edged top surfaces that have slightly diffused walls. This three-parameter control scheme is utilized for a number of immersed boundaries and volumes throughout the domain as seen in Fig. 4.
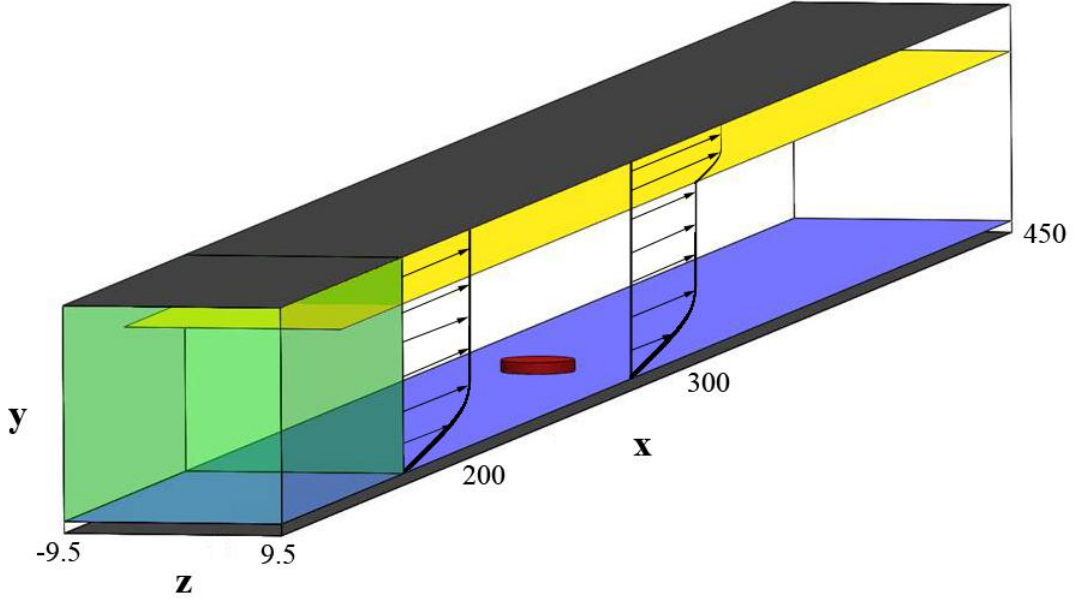

Fig. 4 A schematic of surfaces and volumes forced by the immersed boundary technique. These include the virtual flat plate (blue), suction wall (yellow), buffer zone (green), and cylindrical surface roughness element (red). Numbers are physical values (in mm) of the modeled experiment.[15]

The upper and lower domain boundaries (grey surfaces in Fig. 4) prevent through-flow while still allowing slip. Slightly above the lower boundary a virtual flat plate (blue surface in Fig. 4) is simulated by enforcing no slip and no through flow conditions.

9

Below the plate a small layer of unforced grid points is present (commonly three cells). Any wall normal location is referenced from the virtual flat plate which is at $y = 0$.

Due to the spanwise periodicity of our method, only a single roughness element (red volume in Fig. 4) need be simulated to capture the physics of a periodic array. As with the flat plate, no slip and no through flow are enforced at all grid points defining the element. The roughness element height is restricted to the available wall normal cosine grid spacing. The resulting Re_k values simulated are close to those of previous experiments.[15]

The forcing field also allows for the specification of a boundary layer profile. To closely follow the experimental setup, a Blasius profile is created upstream of the element corresponding to a finite streamwise position. This is accomplished within the buffer zone (green volume of Fig. 4) developed previously by Goldstein et al.[28] Here, flow exiting the downstream boundary is quickly forced back to the desired Blasius profile as it is reintroduced upstream of the element, effectively removing streamwise periodicity. Discontinuities in the flow are avoided by smoothly varying the body force gains through the buffer zone. The velocity gain parameter,

$$\varphi = 20{,}000 \times e^{\left\{-60\left[(x-x_{center})/w\right]^2\right\}}, \tag{2}$$

is exponentially increased to the buffer zone midpoint then decreased through the remainder of the buffer zone. The velocity history parameter θ is zero everywhere except the middle third of the buffer zone where it is similarly ramped up and down

$$\theta = 20{,}000 \times e^{\left\{-6\left[(x-x_{center})/w\right]^2\right\}}. \tag{3}$$

The middle third of the buffer zone essentially makes any remaining flowfield perturbations negligible while the upstream and downstream thirds gently force the incoming and outgoing flow, respectively, to the desired Blasius profile.

Although the boundary layer is much smaller than the channel height it still would not develop as the analytic flat plate solution predicts. Instead, a favorable pressure gradient forms that increases the freestream velocity. Continuity calls for a finite wall normal velocity to be maintained at large distances above the plate,[29] however, this outflow is not permitted by the channel flow configuration of our domain. To help simulate a proper Blasius profile, Strand[30] introduced a suction wall (yellow surface in Fig. 4) into the domain. The forcing field is restricted here to only force fluid in the wall normal direction to the vertical velocity of the Blasius analytic solution. Grid points used for this manipulation extend from the midpoint of the buffer zone to the downstream domain boundary well above the boundary layer.

Rather than converging the entire domain to a steady state as had previously been done, a new procedure was implemented by Strand[30] which takes advantage of the code's spanwise periodicity. A thin domain, only four spanwise grid points, is converged to a steady full field Blasius profile for the three wall normal resolution cases discussed. After satisfactory convergence is reached, the thin domain is laterally cloned as many times as necessary to create the desired full domain. The resulting Blasius domain can then have a roughness element introduced to begin the actual simulation.

C. Computational Details

Our computational domain (see Fig. 4) represents a physical region of streamwise length $x = 300$ mm, spanwise width $z = 19$ mm, and wall normal height $y = 19.5$ mm. The typical number of physical grid points used in simulations are $N_x = 1024$, $N_z = 128$, and $N_y = 128$. Transformation to and from Fourier space gives physical resolutions of 0.195 mm and 0.0984 mm in the streamwise and spanwise directions, respectively. Variation in the wall normal cosine grid produces spacings of 0.0889 mm (at $y = k$) down to 0.0147 mm (at $y = 0$) that define the roughness element. A time step of 1.5×10^{-6} seconds is assumed from prior applications of the code and validated by CFL stability during initial

11

phases of the simulation while temporal gradients are largest. Computations are performed iteratively on eight processors of the Texas Advanced Computing Center IBM Power5 System.

The buffer zone produces an initial Blasius profile corresponding to a physical distance of 200 mm from a flat plate leading edge. In this manner we simulate a roughness element at $x_k = 300$ mm from the leading edge with a 19 mm spanwise center-to-center spacing λ between adjacent roughness elements, matching the setup of EW[15] directly. Experiments utilized a roughness element diameter d of 6.35 mm specifically to excite the $\lambda/3$ component of disturbance energy. A nominal freestream velocity U_∞ of 12.2 m/s is used with a code Reynolds number Re_c of 63,033 to again maintain consistency with experiments. These parameters give a Re_x of roughly 230,000, well below the limit of T-S wave breakdown.

Variations between results of SG,[17] RV,[16] and EW[15] initiated discussions concerning the wall normal resolution of DNS at The University of Texas (UT). The 'bump' structures found by SG in the near-wake velocity contours appeared to have adequate representation in the spanwise direction but only about three grid points captured their wall normal aspects. The current work, therefore, attempts to replicate the previous subcritical case of $Re_k = 202$ using the same mesh presented by SG as well as two additional setups, doubling and quadrupling the number of wall normal mesh points. Unfortunately, our wall normal spacing limits the specific Re_k values we can accurately represent. The nearest values we are able to achieve are 216, 195, and 197 for the $N_y = 128$, 256, and 512 grids, respectively. Initial grid convergence studies are addressed by simulating a well resolved Blasius profile without roughness present.

D. Boundary Layer Verification

While relaxing the thin slice domains, temporally varying structures developed within the boundary layer. After roughly 200,000 time steps, streamwise periodic downward flow 'bubbles' were found along the entire extent of the domain. These structures were a clear misrepresentation of a Blasius boundary layer even though streamwise profiles seemed very close to analytic results. The 'bubbles' had a definite periodicity and movement linking them to a computational issue with the buffer zone. Parameters within Equations 2 and 3 were increased by roughly three orders of magnitude from their previous values to those presented above. The vertical velocity structures were immediately dissipated and a proper boundary layer was produced.

Figure 5 shows extracted velocity profiles from the various N_y domains at the location of the roughness element ($x_k = 300$ mm) prior to initializing its forcing field. Velocities are normalized by U_∞ and wall normal distance by the local δ_{99}. Percent error is computed with respect to the freestream. All cases are shown to produce less than 1% error at any height and little difference is found between the various cases. There is a slight additional error for the $N_y = 128$ (coarse) grid with respect to the others but, it is minimal. The medium and fine meshes produce nearly identical error profiles, except for the magnitude of Gibbs oscillations. Convergence to the Blasius solution verifies the use of the suction wall approach for modeling flat plate boundary layers.
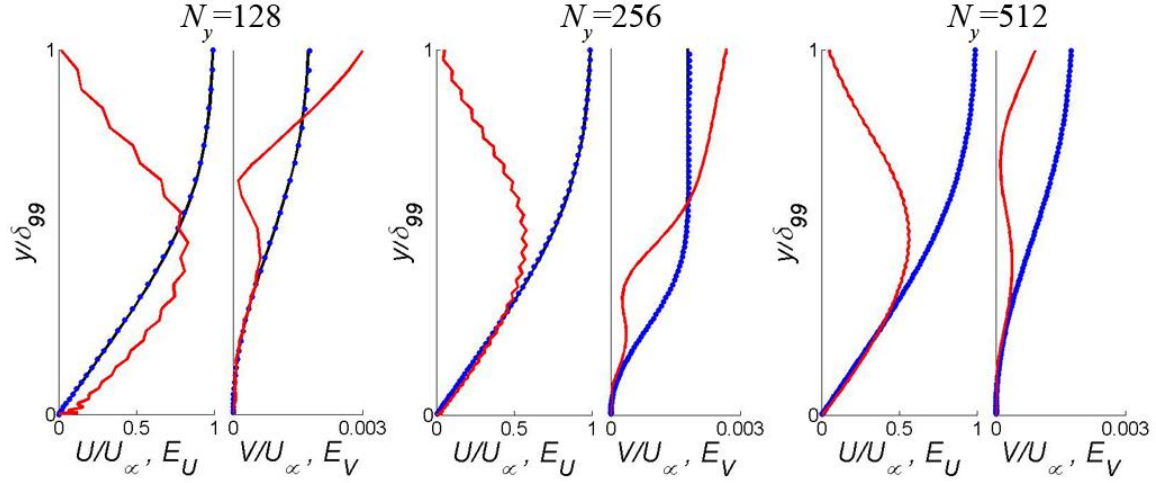
Fig. 5 Boundary layer profiles prior to initializing roughness element forcing. Current DNS (blue symbols) matches the Blasius analytic solution (black line) well, as noted by the local percent error (red line) being less than 1% for *U* and less than 0.005% for *V* in all cases.

The N_y = 128 and 256 cases are further pursued (the 512 domain exceeds our memory limits for full three-dimensional runs) in matched full simulations of individual roughness elements. Once the solid has formed both cases are run for an extended period of time (at least 75,000 time steps). After extensive visualization both results are found to be nearly identical so that only the N_y = 128 case is presented here.

E. Time Variability and Flow Settling

Introduction of the roughness element is an unphysical process in which forcing of the element volume is abruptly turned on. This creates a sequence of time varying flow structures in the domain. Instantaneous forcing essentially 'jerks' the flowfield into a local quasi-turbulent state. Large perturbations propagate downstream and dissipate as they enter the buffer zone. After the flowfield near the roughness element has settled, the downstream recirculation region slowly develops to nearly its final size and shape. At this point, a macroscopic view of the near-field appears to have become steady by standard visualization. Careful examination of downstream velocity contours, however, displays a

14

very slow relaxation of sharp gradients noted only within about two cylinder diameters downstream of the roughness element. Prior DNS studies of similar cases have not quantified the relaxation time required for this type of simulation.[16,31] Fischer and Choudhari, for example, suggested that the flowfield 'looked' similar at widely separated time intervals while Rizzetta and Visbal simply noted the number of iterations before collecting data. For a majority of this work we shall assume that our flowfield has essentially reached steady state due to very similar visualizations generated at times separated by at least 20,000 steps. Time variability of the simulation will be addressed more completely in Chapter 6.

III. COMPARATIVE RESULTS

We first attempt to reconcile differences presented by SG[17] with previous DNS of RV[16] and hotwire experiments of EW.[15] These studies The same DNS code utilized by SG is again carefully used under similar flow conditions with the goal of removing doubt regarding the computational method. Modifications to the current run include implementation of the suction wall, adjustments to the buffer zone, additional relaxation time, and a slight change to Re_c. Comparisons are made with many aspects of the three previous studies.

A. Disturbed Boundary Layer

Figure 6 qualitatively displays the near-field of all three computational simulations. No turbulence is expected given the subcritical Re_k and previous findings. Along the spanwise centerline the structure is similar to that of flow over a two-dimensional sharp-edged object. An upstream separation line and a downstream reattachment line are present that enclose regions of reversed flow. SG noted an extended downstream recirculation region in their simulation as compared with RV which is again the case for current DNS.
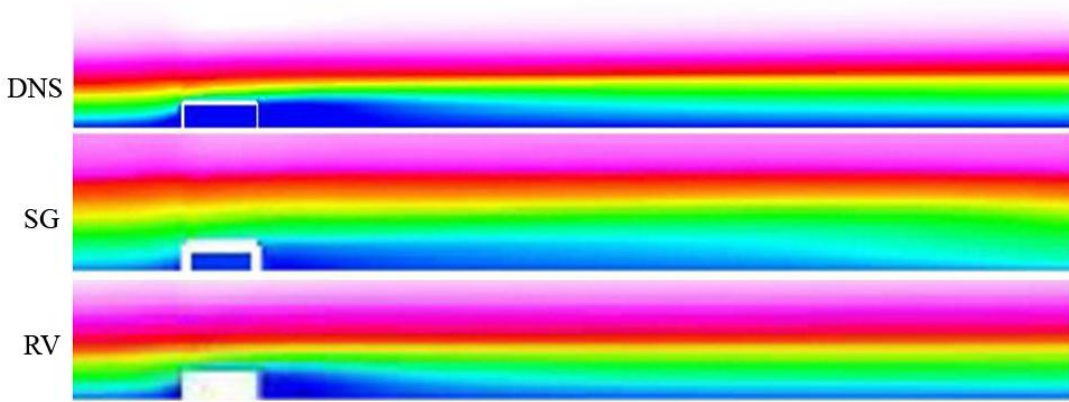

Fig. 6 Cylinder centered boundary layer slices of the roughness element near-field. Contours are of streamwise velocity *U* and the white rectangles denote locations of the roughness elements. Flow is from left to right.

16

To more carefully evaluate characteristics of the roughness element wake, boundary layer profiles are taken at several downstream stations. Figure 7 displays a matrix of these: current DNS, DNS of SG, and DNS of RV plotted with hotwire results of EW. Profiles are extracted from similar downstream locations at roughly $3/2d$, $6d$, and $9d$ downstream of the roughness element center. In all plots two spanwise positions are presented, one centered behind the roughness element ($z = 0$) and the other midway between adjacent cylinders ($z = \lambda/2$).

RV presented their DNS atop hotwire data of EW. Between roughness elements both studies found very nearly the analytic Blasius solution, suggesting that this configuration of $d/\lambda = 1/3$ consists of essentially isolated elements.[15] In the roughness element wake, both RV and EW found similar profiles of slowed flow that reaccelerated as it propagated downstream. The $3/2d$ plot of the RV and EW row shows the physical limitations of the hotwire probe used by EW. The experimental profile at $z = 0$ has a linear profile below about $\eta = 1.0$ as opposed to the reversed flow found by DNS, due to the hotwire probe's inability to read negative velocities. Also, the experimental results do not quite extend to $\eta = 0$, because the hotwire probe size restricts how close to the wall it can reach.

In most cases, SG presented similar results. Spanwise filtering, to be discussed later, is also displayed in these plots but produces little change to the unfiltered DNS data. Reacceleration of the boundary layer is again found downstream as well as a reasonable collapse to the Blasius solution at $z = \lambda/2$. SG simulate a faster boundary layer than the analytic Blasius solution predicts due to a small favorable pressure gradient within their domain; an issue with dimensionalizing the suction wall caused this result and has since been resolved. The $3/2d$ plot of the SG row also finds the region of reverse flow directly behind the roughness element. Similar profiles are again presented of current DNS. Downstream reacceleration, convergence to the Blasius solution between adjacent

17

elements, and reverse flow in the near-wake are all comparable to results of previous studies.
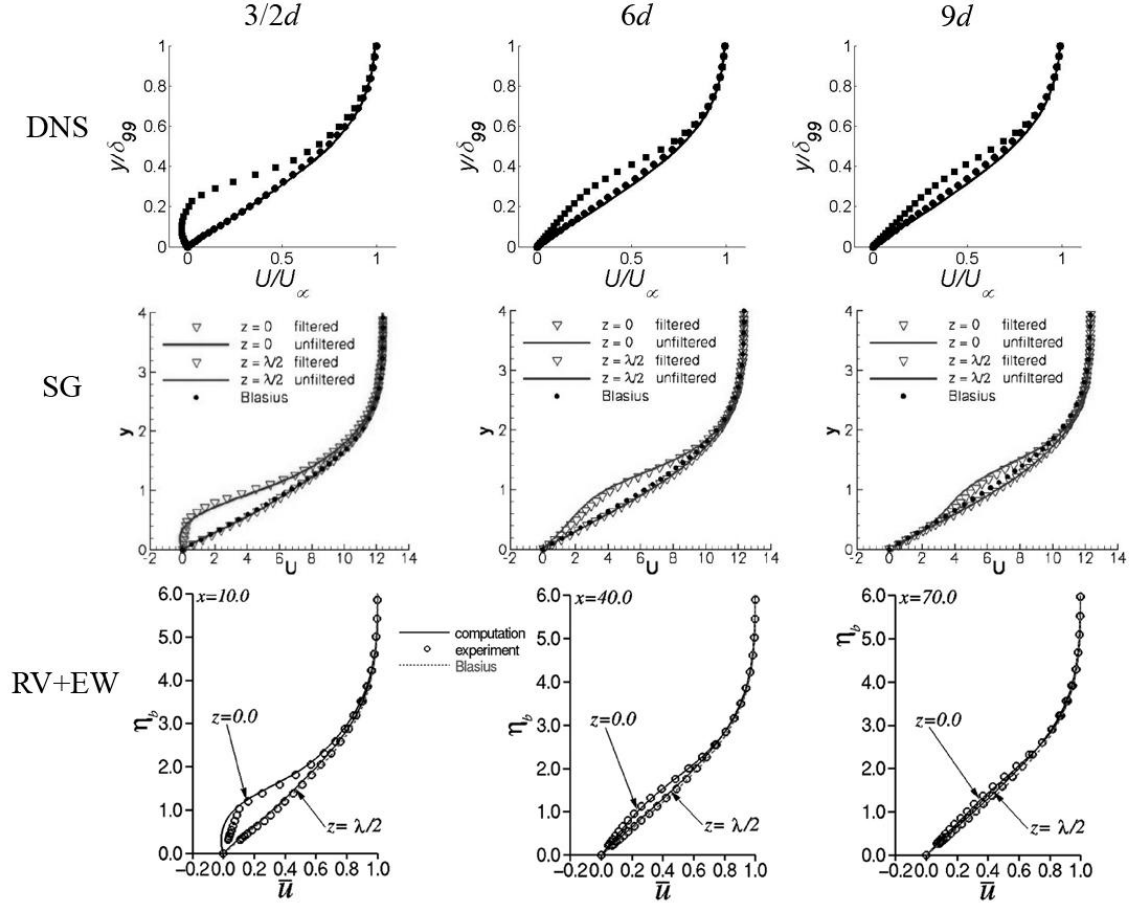

Fig. 7 Disturbance velocity profiles. Rows correspond to studies: current DNS, DNS of SG, DNS of RV with hotwire experiments of EW. Columns correspond to stations downstream of roughness element center: approximately 3/2*d*, 6*d*, and 9*d*. Previous studies are displayed with their respective legends. Current DNS shows the analytic Blasius solution (line), data points between adjacent elements *z* = *λ*/2 (circles), and centered behind the element *z* = 0 (squares).

Two-dimensional streamwise velocity slices are also taken at the same downstream locations of Fig. 7 (3/2*d*, 6*d*, and 9*d*). A matrix of these results is presented in Fig. 8 where it is seen that none of the results exactly match the others. Four 'bumps' were simulated by SG in the near-field whereas only three are currently found with more

18

pronounced lateral gradients. These contour modes are not seen in the RV or EW results. Between relatively undisturbed flow and the central velocity deficit region, similar symmetric high-speed 'dips' are found in all DNS results. Such dips are also displayed in hotwire experiments but the amplitude and corresponding gradients are reduced.

As the flow propagates downstream (to 6*d* and 9*d*) the 'bump' structures of current DNS and SG quickly dissipate. Current DNS matches experimental results quite well at these stations as the velocity deficit region takes on a triangular shape, consistent with spanwise alternating high and low speed streaks. Neither DNS of SG nor RV matches this result as their velocity deficit regions maintain rounded profiles. The wake of SG seems to be compressed and stretched in the spanwise and wall normal directions, respectively. All other cases, though, maintain very similar contour amplitudes with respect to one another. The symmetric 'dip' structure on either side of the velocity deficit profile is now found in all cases with slight differences in the severity of gradients.
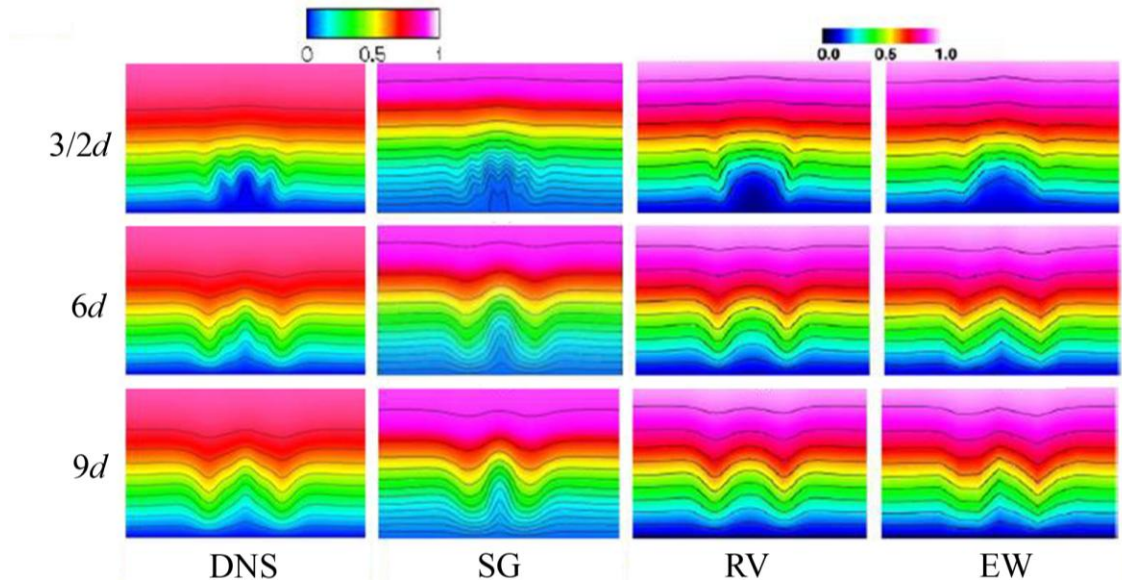

Fig. 8 Instantaneous streamwise velocity contours at roughly 3/2*d*, 6*d*, and 9*d* downstream of roughness element. Figures are stretched about four times in the wall normal direction to better display gradients. Lines are 10% increments of freestream velocity.

To help visualize the discussions of Figs. 7 and 8 current results are presented together in Fig. 9. Here the cylindrical roughness element is displayed with the local DNS domain, boundary layer profiles of Fig. 7, and velocity contours of Fig. 8.
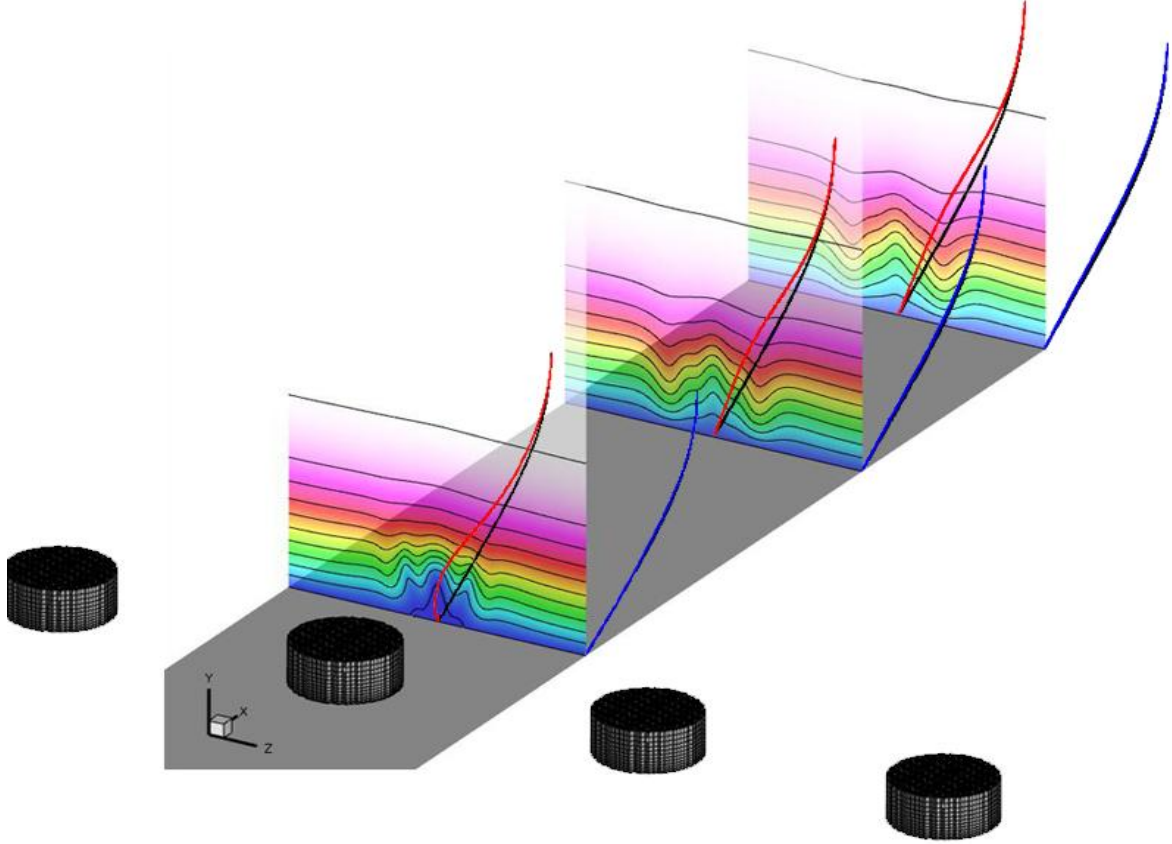

Fig. 9 Local domain of current DNS. Flow structures downstream of the roughness element are presented by velocity contours and boundary layer profiles. The Figure is stretched about four times in the wall normal direction. Downstream stations are at roughly 3/2*d*, 6*d*, and 9*d* and boundary layer profiles are presented at spanwise stations of z = 0 (red) and z = λ/2 (blue). Lines within velocity contours are 10% increments of freestream velocity and black boundary layer profiles are of the undisturbed analytic Blasius solution.

B. Vorticity

Current DNS finds three vortex cores upstream of the roughness element (see Fig. 10). Streamlines are found to diverge from the cylinder surface stagnation point (S_1) at a

20

location slightly below the top leading edge of the roughness element. The flat plate stagnation point (S_2) is upstream less than $1d$ of the cylinder center. These aspects of the flow are representative of two-dimensional flow over a sharp-edged surface mounted object. Vortex cores and the saddle points between them mark the upstream line of zero U (further referred to as the recirculation line). This line represents a bounding surface where incoming flow interacts with the surface roughness and is turned upstream. The vortex cores entrain slow moving fluid from this region and eject it around the sides of the cylindrical element in a manner similar to juncture flow. All ejected fluid follows a path specific to the vortex core it stems from so that further visualization involves placing a single streamtrace at the three vortex singularity points.
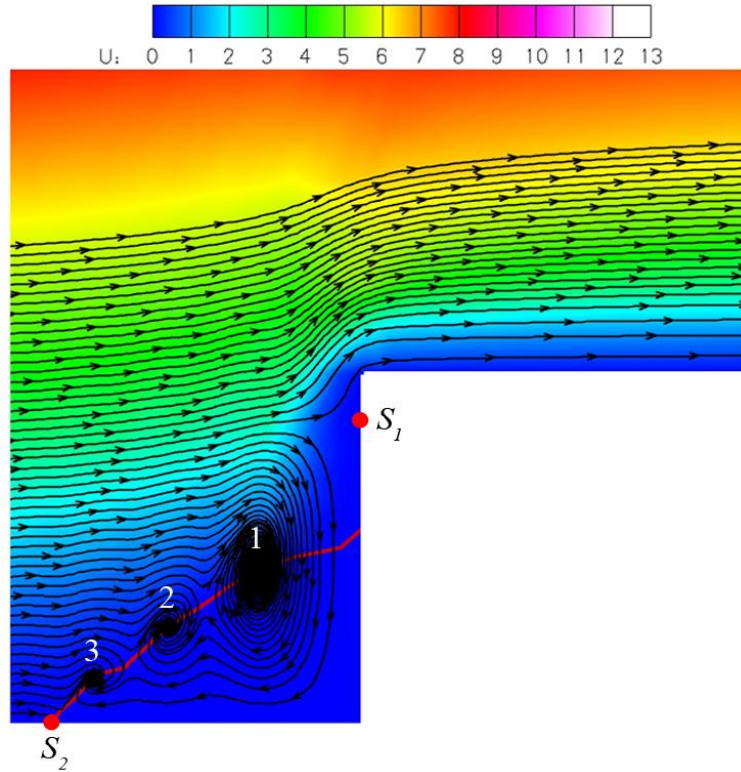

Fig. 10 Upstream vortex core topology. Streamwise velocity contours are shown on the symmetry plane of the domain. In plane streamlines (black) are used to visualize boundary layer interaction with the surface roughness (white). Stagnation points and the recirculation line are marked in red. Numbers indicate upstream vortex cores to be referenced further.

21

Three-dimensional vortex systems stemming from the upstream recirculation line are shown from all three DNS studies as red streamtraces propagating downstream from the upstream vortex cores like those of Fig. 10 (see Fig. 11). Current DNS finds three vortex legs similar to those of SG while RV found only two pairs. In all cases the primary vortex core, the largest and closest one to the roughness element, develops into a simple horseshoe system. Both legs wrap around the sides of the cylinder and propagate directly downstream outside of the disturbed wake. The secondary vortex cores create trailing systems in all cases that wrap around the cylinder sides, recirculate upstream behind the element, and then turn directly downstream. The downstream point at which the secondary pair turns upstream is closest to the element in the SG study and furthest in the current work. The third and smallest upstream vortex core creates another set of recirculating trailing legs. Recirculation of this pair occurs further upstream, further from the spanwise centerline, and in a shorter total distance than with the secondary pair.

Slices downstream of the element in Fig. 11 display magnitude of streamwise vorticity $|\omega_x|$. It was expected that the largest vortex core and corresponding legs of the horseshoe system would produce the highest levels of vorticity downstream, but this is not the case. Instead, minimal vorticity is found where the primary horseshoe streamlines cross the downstream planes. This is due to the relative weakness of the collar vortices and the majority of $|\omega_x|$ being generated by the shear layer on top of the roughness element.[16] In the furthest upstream slice all simulations find the highest levels of streamwise vorticity below the vortex streamtraces, very near the wall, at spanwise stations corresponding to the roughness element edges. RV find another high concentration of $|\omega_x|$ between legs of the secondary vortex and legs of the primary horseshoe system. Current results and SG find similar regions surrounding locations where the tertiary vortex streamtraces cross the first downstream plane. Given the lack of a tertiary vortex system in the RV case, it seems likely that this region of increased $|\omega_x|$ is again primarily caused by the element's

22

top shear layer and not by the trailing system itself. In all cases minimal vorticity is found along the cylinder centerline and the overall magnitude dissipates quickly downstream, noted by the lack of strong contours in the furthest downstream slice.
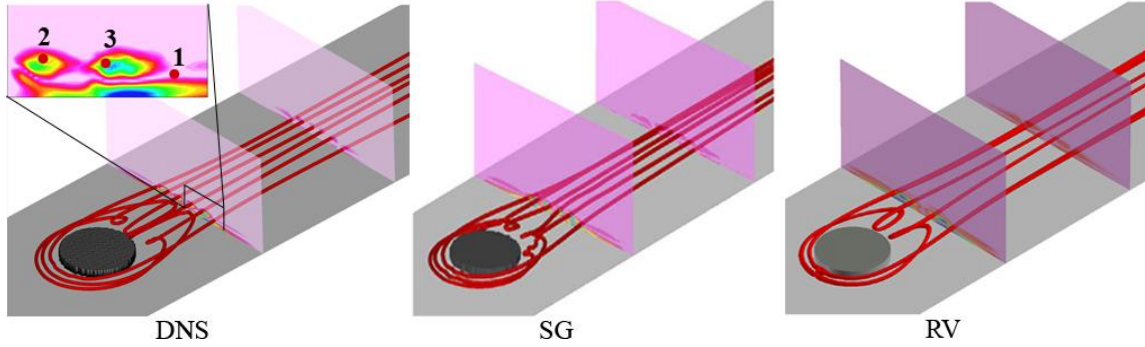

Fig. 11 Vortex systems. Red tubes display streamlines stemming from vortex cores upstream of the roughness element. Downstream slices are contoured by the magnitude of streamwise vorticity $|\omega_x|$ and are located approximately 3/2d and 4d downstream of the element. The number of vortex cores simulated varies by study: three by current DNS, three by SG, and two by RV. Red dots in the two-dimensional view of current DNS mark where vortex streamtraces penetrate the first slice.

The variations presented here display how complex the flow about surface roughness is and the challenge of accurately simulating it. Differences between experimental and simulated results can be expected under the circumstances of imperfect testing conditions and imprecise computational inputs, and can often be corrected for. It is troublesome, though, to find such disagreement between computational efforts that are calculating results from essentially the same fundamental equations. Addressing these issues was the initial motivation of this work and will be discussed in the following section.

IV. RESOLVING ISSUES

A. Downstream Velocity Contours

Resolution of the hotwire experiments was initially questioned by SG. It was noted that the 'bump' structures found by DNS in the near-wake velocity contours were smaller in the spanwise direction than the 1.25 mm (about $1/5d$) hotwire probe used. DNS data points were mapped to the *experimental* grid by averaging several adjacent cells that would fall within the physical acquisition volume of the hotwire probe. The resulting filtered data were then found to match experiments very well.

The same filtering procedure is applied to current DNS and found to produce similar results. Figure 12 shows filtered results from current DNS and those from SG. Filtering the first downstream slice does not completely eliminate the 'bump' structures as before with SG, due to the stronger lateral gradients present. Filtering does, however, significantly reduce these contour modes, matching experimental results well in shape and magnitude.

As mentioned previously, further downstream contour slices of SG become slender in the spanwise direction and no longer match experimental findings. Current DNS on the other hand, matches the downstream shape with a complete reduction of 'bumps,' showing excellent agreement with experimental results. This is an important result as data sets outside of the immediate downstream disturbance wake are of primary interest. The current theory neglects non-linear and non-parallel flow characteristics present in the near-wake of the roughness element. Therefore, decomposition and reconstruction is usually only valid aft of the roughness element near-wake, about $4d$ for this configuration.[14]
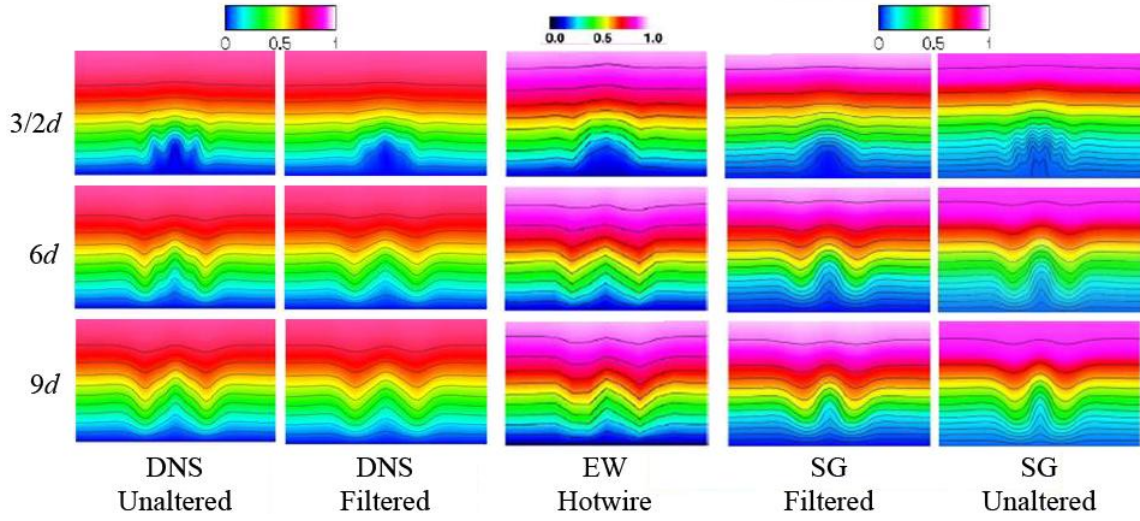
Fig. 12 **Streamwise velocity contours at roughly 3/2*d*, *6d*, and *9d* downstream of roughness element. Lines of current DNS and EW are 10% increments of freestream velocity.**

B. Vortex Topology

We next compare the upstream flow topology to juncture flow visualization experiments performed by Baker[20]. His study used smoke filaments to visualize the upstream vortex topology of circular cylinders mounted in a flat plate laminar boundary layer. The configurations tested involved cylinder heights roughly two times the local boundary layer thickness whereas k in the current study is about 1/5 of δ_{99}. Nonetheless, visualizations of the three DNS studies presented have all shown characteristics similar to juncture flow.

Baker found a number of upstream vortex topologies dependent upon non-dimensional flow and geometry parameters. He notes three steady topologies consisting of two, four, or six upstream vortex cores. In every situation half of the vortex cores are located along the upstream recirculation line and the other half (the smaller ones) are found counter-rotating below their counterparts. Stemming from the recirculation line vortex cores are counter-rotating vortex legs that develop around the cylinder. A horseshoe vortex system

25

is always produced by the vortex core closest to the cylinder and recirculating trailing vortex systems stem from any additional upstream cores. [21]

RV presented a horseshoe vortex system along with a single trailing system, suggesting the four vortex core topology found by Baker (see Fig. 13). Current DNS finds similar results to RV but with an additional trailing system, corresponding to the six vortex core topology. The three recirculation line vortex cores found in current DNS and SG are expected to be correct because the configuration of all three studies lies well within the six core regime characterized by Baker.
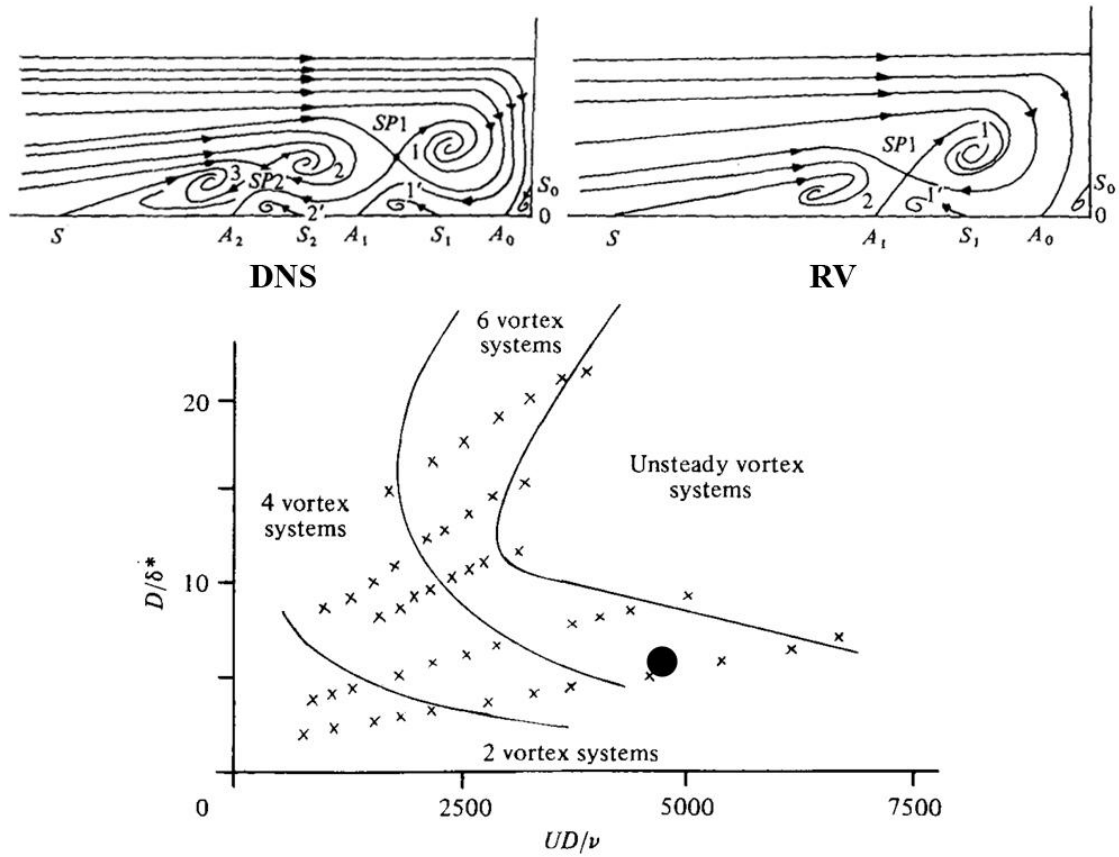

Fig. 13 Upstream vortex topologies. Schematics of the six and four vortex systems presented by Baker[20] correspond to the results of current DNS and RV, respectively. However, current DNS results are expected to be correct as marked on Baker's plot.

26

C. Experimental Considerations

Flow visualization experiments at UT are used to further examine these near-field flow structures. Laser doppler anemometry (LDA) is performed with a Dantec FlowLite 2D system in a low speed Eidetics 1520 water channel. A 10 mW 632.8 nm Helium Neon laser is used to acquire streamwise velocity measurements of the polyamide seeded flowfield. The acquisition volume of this system has spanwise and wall normal resolutions of 5.032 mm and 0.239 mm, respectively. The two-dimensional grid used produces excess spanwise sampling as it has a constant step of 0.5 mm (the wall normal step is consistent with the acquisition resolution at 0.25 mm). A finer contour of only the velocity deficit region is also produced and overlaid onto the coarser mesh. The LDA system is known to have a relative measurement uncertainty of less than 2.1%.[32] Preemptive boundary layer measurements are found to be within 3% of the analytic Blasius profile and are likely due to a small freestream velocity gradient along the streamwise extent of the test section. Freestream turbulence levels U_{rms}/U_∞ have been recorded in prior experiments between 1 and 1.5 percent of the freestream velocity.[32]

A single cylindrical roughness element is created which matches the non-dimensional geometry k/d of EW. Flow properties, Re_x and Re_k, are also consistent with those of EW in the water channel flat plate configuration currently used. Experimental parameters are therefore $k = 1.359$mm, $d = 12.156$mm, $x = 583$mm, and $U_\infty = 0.37$m/s. The LDA system has similar spanwise and wall normal resolutions as the hotwire probe used by EW and thus produces very similar results. Figure 14 shows a side by side comparison of the $3/2d$ downstream velocity contour from both sets of experimental data. A semi-triangular velocity deficit region is found with the same overall shape and size as in EW, again suggesting the need for sufficient spanwise resolution to properly capture the smaller flow structures.
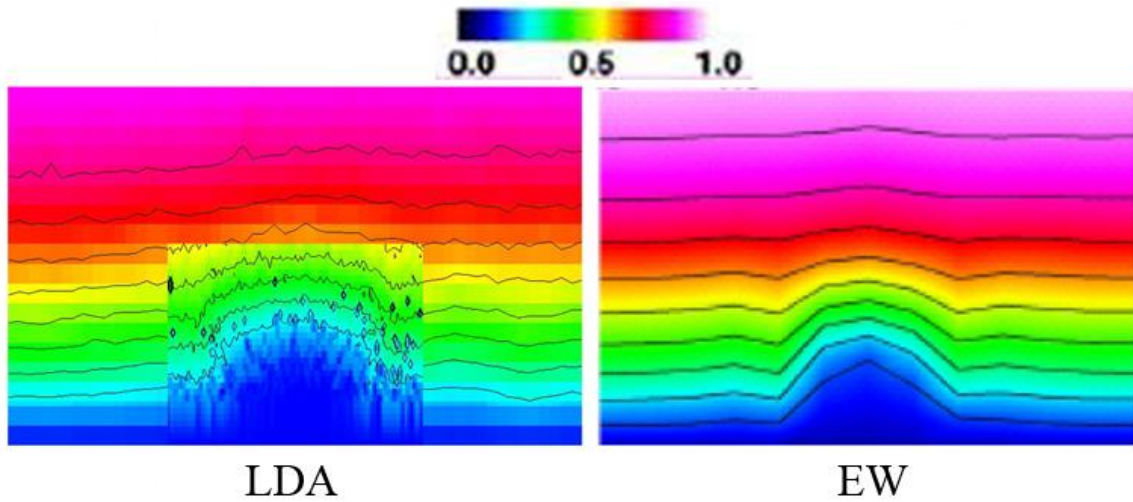
27

Fig. 14 **Experimental comparison. LDA performed at UT is found to match hotwire experiments of EW due to similar spanwise and wall normal resolution. The insert of the LDA data is from a finer measurement mesh superimposed onto a coarser one.**

Dye injection in water is also used to help verify the vortex systems present. The flow structure may be slightly varied by this visualization technique due to the dye having a different density than water and the weak effusing jet created as dye is injected upstream of the element. To minimize these effects, dye is injected into the boundary layer very slowly. Figure 15 shows both a side view and a top down view of the near-field flow structure displayed by this technique along with similar surface streamlines and vortex streamtraces of the current DNS. The side view clearly shows the location and size of the upstream primary vortex core along with the corresponding fluid ejected around the element. The downstream recirculation region is found to be difficult to visualize due to diffusion of dye throughout the slow moving volume.

The top down view is more useful for visualizing a number of flow structures. Red dye injected in the upstream recirculation region is collected by the primary vortex core and ejected around the element sides as a horseshoe system. Just downstream of the element sides a small amount of red dye is found creeping upstream towards the lateral separation

28

points (A). An arc of fairly stagnant red dye (B) is also found on the surface slightly offset from the element's trailing edge. The remainder of the aft recirculation region is again blurred although its overall shape and size are captured. Downstream of the $3/2d$ plane three streams of red dye are found to progress off the surface at locations corresponding to the three vortex streamtraces. Entrainment of dye at these locations may indirectly verify the upstream vortex topology predicted by juncture flow experiments and current DNS.
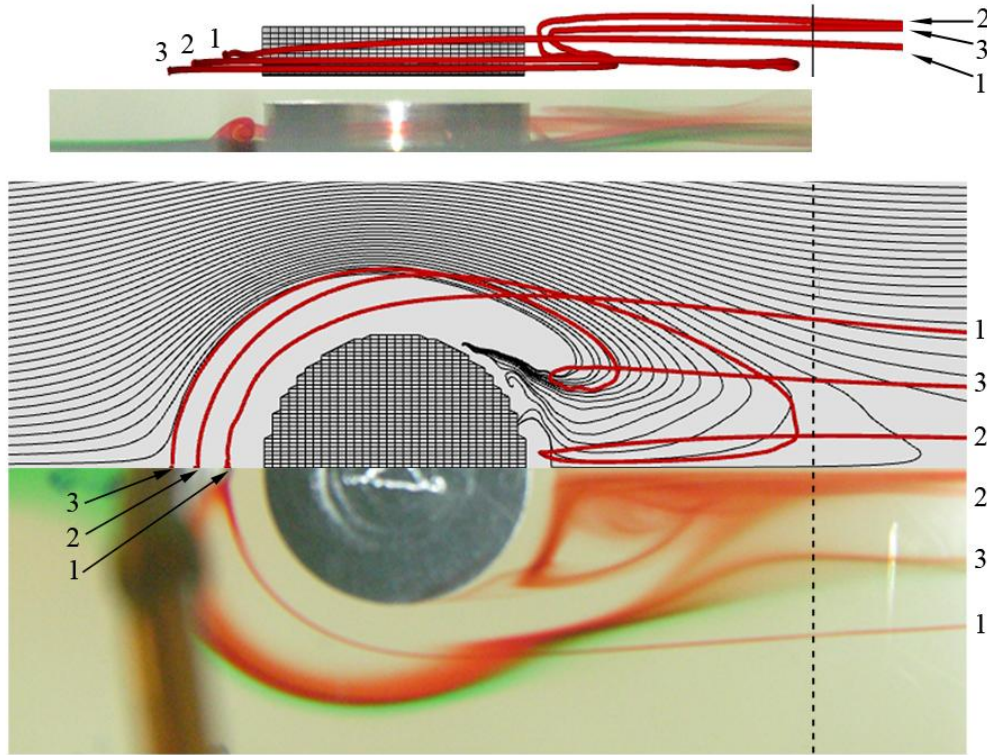

Fig. 15 Flow visualization comparisons viewed from the element side and from above the element. Flow structure of DNS (top) is matched with dye injection in water (bottom) for both perspectives. Numbers indicate locations of the primary, secondary, and tertiary vortex systems that propagate downstream from the upstream recirculation line vortex cores. The brown structure upstream of the cylinder is the dye injection port on the opposite side of the flat plate. The line marks the location of the $3/2d$ downstream slice. Flow is from left to right.

V. NEAR-FIELD STRUCTURES

Detailed flow visualization of current DNS is now presented to describe near-field structures produced by these roughness elements. Specifically, how the downstream velocity contour 'bump' structures are generated and contributions of the vortex systems to the surrounding flowfield are examined.

A. In-Plane Velocity and Streamwise Vorticity

The U contour taken 3/2d downstream of the roughness element displays the largest lateral gradients of any of the slices presented and is within the non-linear region of the wake described by Denissen et al.[14] Figure 16 displays contours of ω_x, lines marking 10% increments of U_∞, arrows indicating in-plane velocity, and markings of where vortex streamtraces cross the plane.

As mentioned above, $|\omega_x|$ contours do not seem to correspond directly to the primary horseshoe vortex system swept downstream of the roughness element. This is again displayed by the lack of strong vorticity and in-plane vector swirl where the horseshoe streamtraces cross the plane (spots labeled 1). On the other hand, locations of penetration by the secondary and tertiary systems are roughly marked by in-plane vectors wrapping around them and slightly offset but, strong vorticity.

It can be seen that there is a strong correspondance between in-plane velocity and the U contours. The symmetric high-speed regions that cradle either side of the velocity deficit have a large influx of fluid from flow outside of the roughness element wake. Relatively undisturbed flow between adjacent elements is moved laterally inward as the wake contracts and high-speed flow from the upper boundary layer is brought downward to produce the 'dips.' This inflow is also seen from the upper boundary layer at the 'dips' between legs of the secondary and tertiary vortex cores. The local flow speed is increased at these locations with respect to the adjacent 'bump' structures as incoming U is greater

30

than the locally retarded velocity. It seems then that the lateral gradients of the downstream U contours are an effect of the increased local flow speed (the 'dips') and not a local decrease of flow speed (the 'bumps'). Removing the 'dip' structures and smoothing the contours from peak to peak would result in a velocity deficit profile much like those of EW.
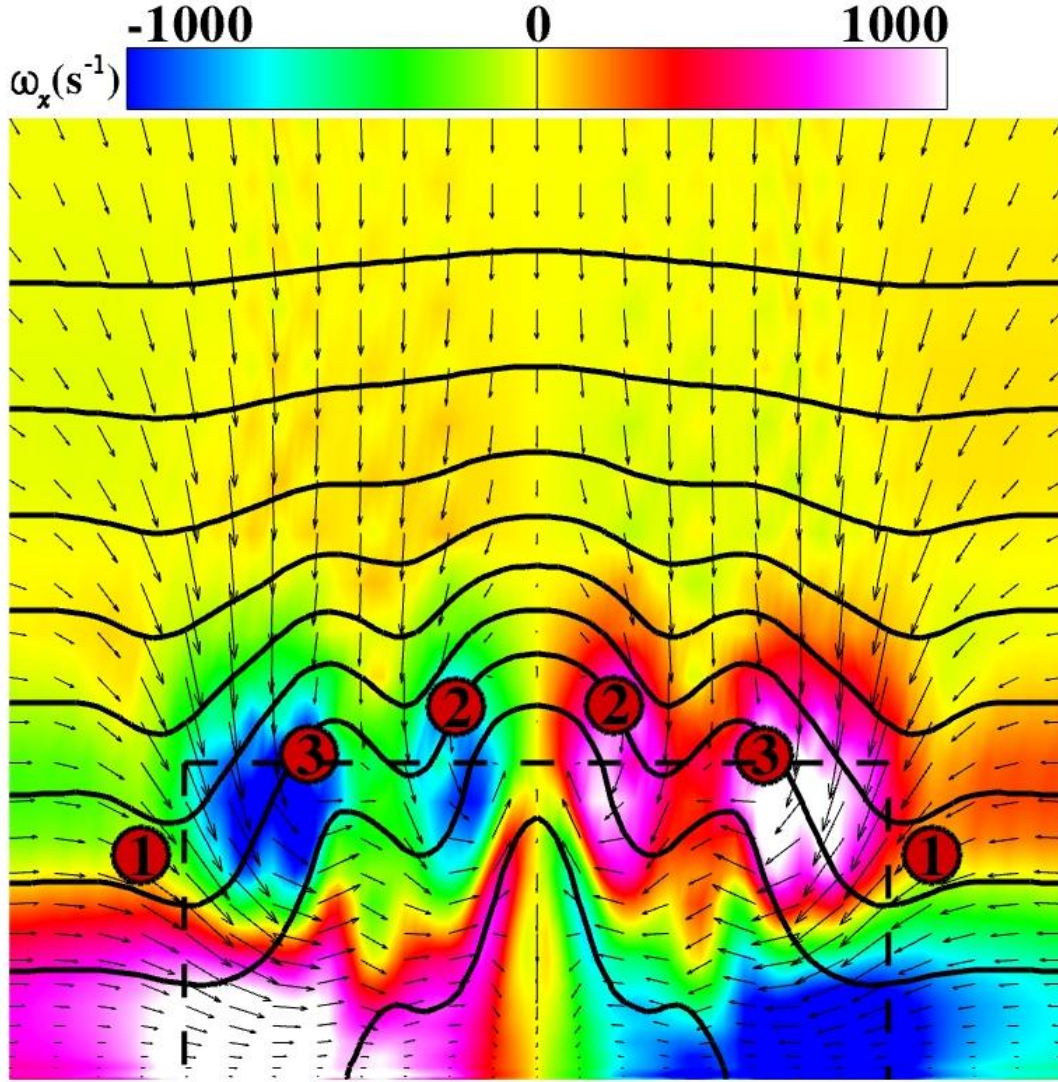

Fig. 16 Close-up contours of ω_x 3/2d downstream of the roughness element (dotted line). Lines are 10% increments of U_∞. Arrows indicate in-plane velocity. Red dots mark where vortex streamtraces penetrate the plane. The view is a close-up of the near-wake stretched about four times in y.

31

B. Vortex Systems

We next examine flow about the roughness element in terms of the three-dimensional near-field. First, the upstream recirculation line vortex cores of Fig. 8 are used to visualize vortex propagation about the cylindrical element. Streamtraces are introduced in the three-dimensional domain at the singularity points of each upstream vortex core (see Fig. 17). As previously described, a horseshoe system (stemming from the primary vortex core) and two additional trailing systems (stemming from the secondary and tertiary vortex cores) are found.

A rake of streamlines is also placed on the top surface of the roughness element to visualize how the top shear layer interacts with the near-field. Upstream propagation of these streamlines is noted in Fig. 10 by the first streamline to progress over the element above S_1. At the trailing edge of the roughness element spanwise divergence of the streamsheet occurs. This splitting was initially thought to be associated with the discreteness of the element's cartesian representation. In Fig. 17, though, it seems that recirculation of the secondary and tertiary trailing systems corresponds to this lateral divergence of the top shear layer. When either vortex streamtrace is turned from the upstream to the downstream direction, it is surrounded by large amounts of the local fluid. The top surface shear layer is enveloped around the now downstream oriented vortex streamtraces and propagates directly through the U contour 'bump' structures.

As the top surface streamsheet leaves the element's trailing edge it immediately begins to wrap around the vortex streamtraces. This circulation is consistent with the ω_x orientation seen in the $3/2d$ downstream slice, linking the roughness element top shear layer with the downstream lateral gradients. Spanwise vorticity generated over the top surface of the roughness element is reoriented to the streamwise direction as flow leaves the trailing edge. Therefore, it seems that the roughness element's top shear layer produces the

32

overall U deficit profile and its lateral splitting redistributes ω_x in the wake, shaping the velocity deficit contours.

It was noted previously that the largest and strongest regions of ω_x seen in the 3/2d slice (those very near the wall and oriented *opposite* of the secondary and tertiary systems) do not correspond to any of the vortex systems. A group of streamlines are now placed within one of these strong contours and allowed to propagate upstream and downstream. It can be seen that these regions of strongest ω_x are associated with flow near the wall that diverts around the roughness element well away from the vortex streamtraces. The lower boundary layer is spread laterally around the element and then collapses back into the wake. High spanwise velocity is therefore found downstream of the element, creating streamwise vorticity due to the shear layer formed by interaction with the flat plate (further visualized in Fig. 18). These regions of highest ω_x are oriented opposite to the areas of strong ω_x associated with the tertiary trailing system. Lateral flow into the wake is, therefore, found between these two regions (the cradling 'dip' structures previously discussed). As the flowfield progresses past the downstream recirculation region, areas of strong ω_x stemming from the lateral displacement of flow around the element quickly vanish because fluid is again oriented almost completely downstream.

Figure 8 displayed a reduction of lateral gradients in downstream U contours as the flow progressed further aft of the roughness element. Strong regions of ω_x generated by the top shear layer in Fig. 17 are found to dissipate as well and quickly merge together. Fluid is then no longer moved from the upper reaches of the boundary layer into the wake between the secondary and tertiary vortex streamtraces. Instead, it is directed into the wake entirely through the cradling high-speed 'dip' structures. These contours display the typical high and low-speed streaks found downstream of surface roughness.

33

The furthest downstream velocity contours displayed in Fig. 8 all show an increase of magnitude in the cradling 'dips' throughout the entire boundary layer. Although ω_x developed on the top shear layer dissipates as the wake progresses downstream, it continues to bring high-speed flow of the upper boundary layer towards the wall on either side of the velocity deficit. This is likely an effect of strong downward forcing in the near-wake (produced by ω_x) slowly diffusing into the upper boundary layer further downstream of the element. Regardless, the effects of ω_x generated by the roughness element top shear layer are prominent for large downstream distances.
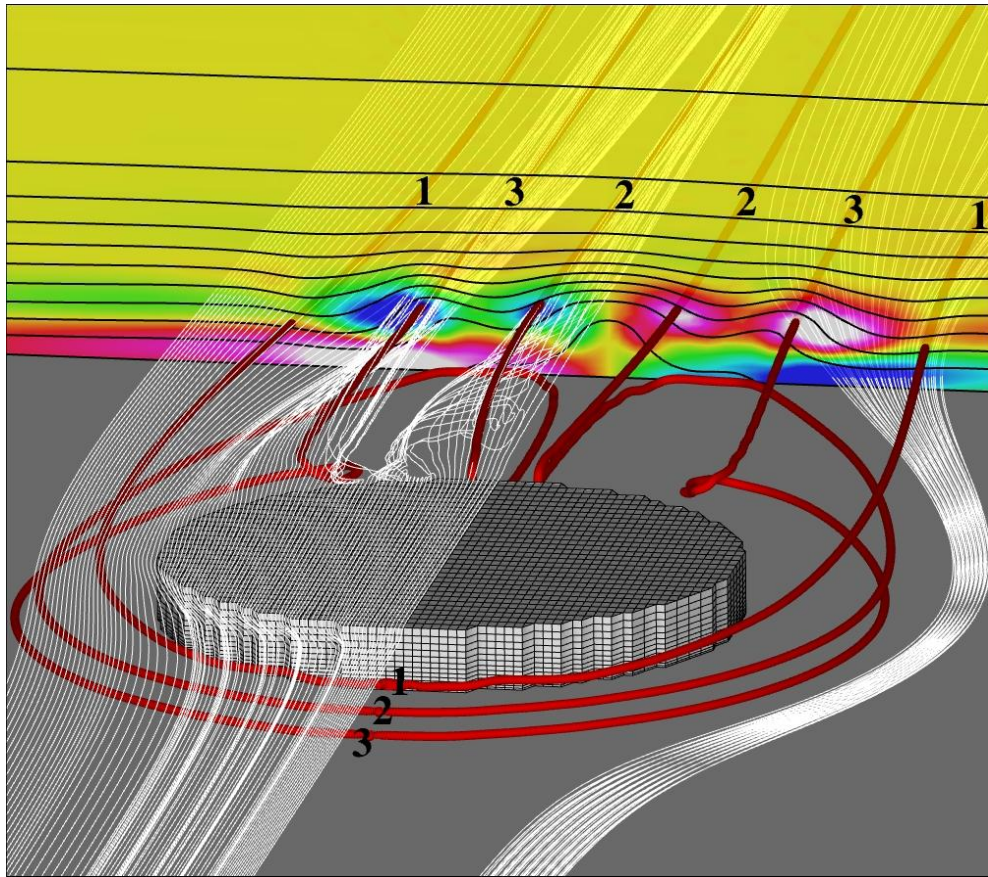

Fig. 17 Streamtraces and the downstream slice of ω_x at 3/2d. Red tubes indicate streamtraces stemming from upstream recirculation line vortex cores. White streamlines are placed on the top surface of the roughness element as well as in a region of strongest ω_x and allowed to develop in both directions. The downstream slice is the unstretched contour of Fig. 14 without vectors. Numbers indicate streamtraces stemming from the corresponding upstream vortex cores.

C. Vorticity Interactions

Similar contour slices of ω_x are presented in Fig. 18 throughout the roughness element near-field. Exaggerated in-plane velocity profiles are also placed well away from the element to help characterize how ω_x is developed by spanwise flow.

Slices A, B, and C all display high levels of downstream-oriented vorticity very near the wall spanning much of the domain half-width. Vectors indicate that this region is produced by the lower boundary layer spreading laterally around the roughness element. The large area of positive ω_x is generated slightly upstream of slice A and can be seen to progressively spread in the wall normal direction through slice C. Downstream of C this region lifts away from the surface and ultimately dissipates outside of the disturbance wake. An upstream-oriented region of strong ω_x, produced by lateral convergence of the lower boundary layer, causes this lift-up. The area of negative ω_x also dissipates quickly but never leaves the surface. Quick dissipation of the positive ω_x region of slice A is likely an effect of lifting away from the surface and into higher-speed boundary layer regimes. Iso-surfaces of these regions are displayed in Fig. 19 to better visualize their development.

Upstream oriented ω_x is found in slice B of Fig. 18 where flow within the recirculation region is ejected from the primary vortex core around the element. Very strong ω_z is produced by spanwise vortex line stretching along the element's centerline (the vortex cores of Fig. 10) and is turned to an upstream orientation as the flow progresses laterally. Neither the secondary nor tertiary core streamtraces correspond to upstream vorticity of slice B as positive ω_x from lateral spreading of the lower boundary layer has overwhelmed reorientation of their minimal levels of ω_z.

Following the primary vortex core streamtrace leads us to an unexpected result. As the upstream recirculation region around the primary core is turned around the element, its

vorticity is reoriented to the upstream direction (negative ω_x region in slice B). Here only the primary horseshoe system corresponds to this vorticity orientation, which it maintains through slice C. Thereafter, positive ω_x near the wall completely dissipates the region of negative ω_x surrounding the primary vortex streamtrace. The primary vortex core streamtrace continues through areas of downstream oriented ω_x (slices E and F) and leaves the field of view with negligible vorticity at the $3/2d$ plane. This change from negative to positive vorticity is inconsistent with a typical vortex system. In this instance then, it seems the streamtrace stemming from the primary upstream vortex core (as seen in experimental flow visualization of Fig. 13) is ultimately not a coherent vortex system at all but, rather, merely a passive tracer of fluid ejected from the upstream recirculation region. The horseshoe streamtrace legs of the primary vortex core likely have very little affect on the flow field downstream of the surface roughness. This result is contradictory to the often-suggested boundary layer reorganization mechanism associated with the primary horseshoe system.[1,2,5,8] The secondary and tertiary vortex cores produce similar passive tracers as their streamtraces alternate vorticity orientation in the same manner as the horseshoe system.

By suggesting that the secondary and tertiary vortex streamtraces are passive it appears that they are not driving the lateral divergence of the top shear layer. Instead, recirculation of either system downstream of the roughness element allows vorticity departing the trailing edge to capture them along with the top streamsheet. This occurs when the upstream-oriented streamtraces encounter the roughness element aft face and progress upward towards the exiting top shear layer. It appears then that flow leaving the trailing edge is capable of influencing fluid below it very near the plate surface.

Weak downstream oriented vorticity is found in slices C and D on the top surface of the roughness element. This is due to lateral flow seen in the streamsheet of Fig. 17. The convoluted nature of the top shear layer diverging at the trailing edge and entering the

near-wake can be seen in slice E. Directly downstream of the element multiple regions of alternately oriented vorticity are found in very close proximity to one another. Reorganization of these regions quickly occurs by slice F where two high intensity areas of positive ω_x are found progressing downstream. At the furthest downstream stations ω_x generated by turning of the top shear layer is found to dissipate much slower than regions produced by the lateral spreading of the boundary layer. This continued propagation of vorticity within the wake maintains the high-speed regions cradling the centered velocity deficit. Therefore, the spanwise alternating high and low-speed streaks commonly found downstream of surface roughness may not be the result of horseshoe vortex systems at all; rather, streamwise vorticity from the reorientation of the top shear layer is likely the primary cause.
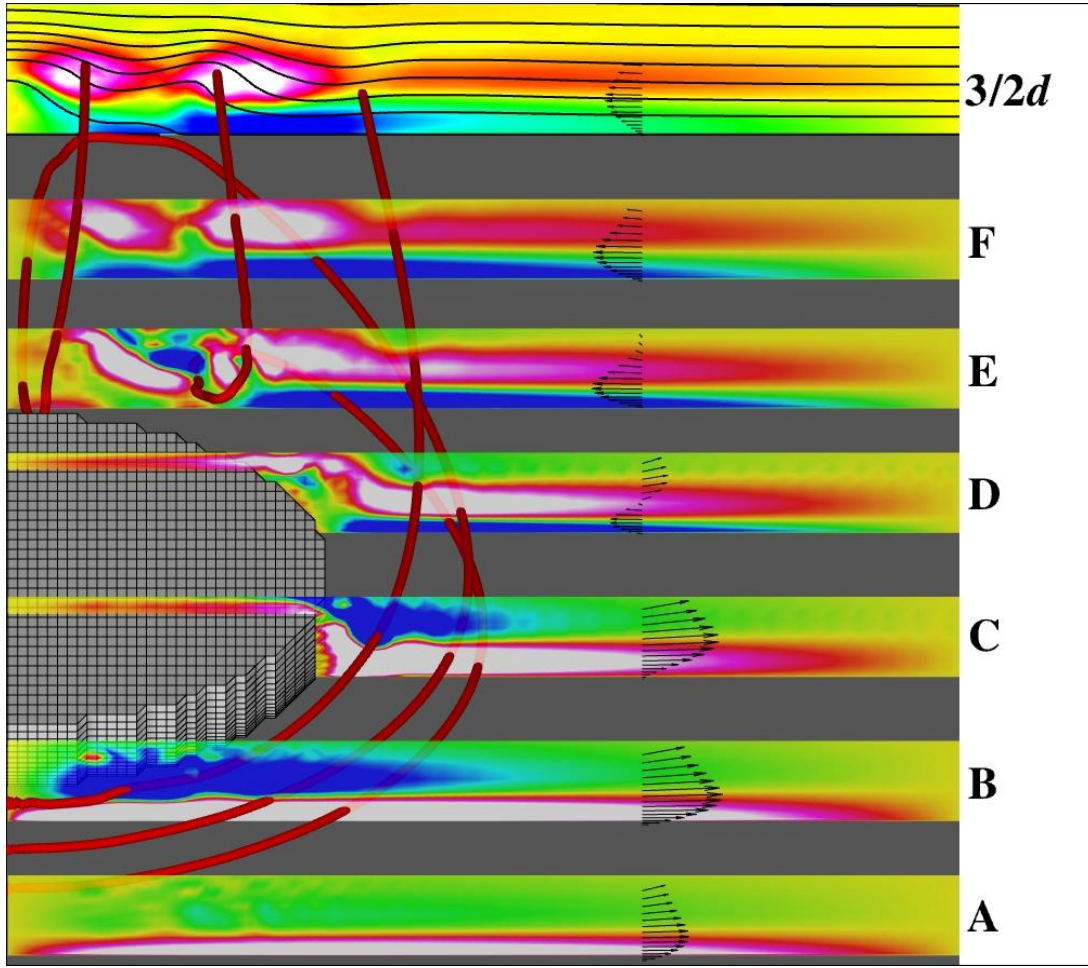
Fig. 18 Spanwise slices of ω_x progressing through the near-field. Slices are ordered in the streamwise direction, ending with the 3/2d downstream contour. Vectors display in-plane velocity approximately 1d laterally from the element center. Contours and streamtraces are the same as Fig. 15.

Figure 19 displays iso-surfaces of ω_x that stem primarily from the lateral spreading of the lower boundary layer. The volumes generated upstream of the element are found to overlap the oppositely oriented volumes produced downstream. This interaction occurs at x_k and is described in Fig. 18 when the region of positive ω_x lifts off the surface at slice D. Additional volumes are found where ω_z from the upstream recirculation region is turned around the element along with the horseshoe system. Very small regions are also

38

noted at the element leading and trailing edges that correspond to discreteness of the cartesian representation of the cylinder.

Recent simulations have altered the element discreteness by bulging one half of the trailing edge outward. The stair step pattern at the trailing edge is therefore altered slightly so that splitting of the top shear layer is moved laterally to the new step location. Initial flow visualization has displayed a reduction of the $3/2d$ contour 'dip' in the adjusted half of the domain while the unaltered side remains as displayed above. This could potentially be useful for minimizing the near-wake lateral gradients although further investigation is required.

Streamtraces of the upstream vortex cores are now contoured by $\boldsymbol{\omega \cdot U/|U|}$ to display strength of vorticity directed along their paths. Upstream of the element all streamtraces display the expected vorticity orientation and intensity as noted by their size in Fig. 10. As the streamtraces progress around the element, though, all are found to transition to the opposite orientation. This result is not representative of a simple vortex filament, further suggesting that streamtraces here are simply passive tracers.
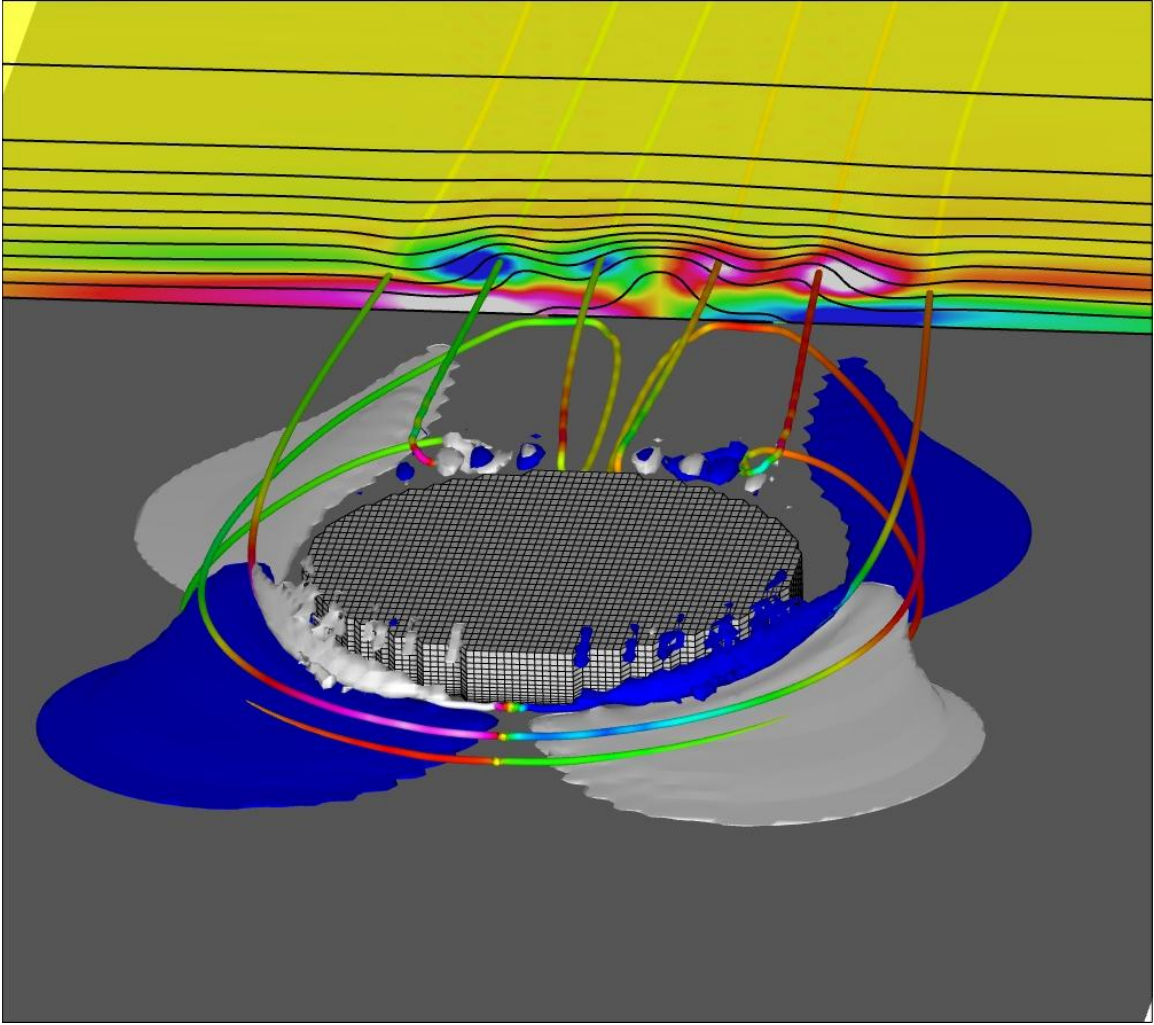
Fig. 19 Iso-surfaces of ω_x and vortex streamtraces colored by ω·U/|U|.

D. Recirculation Volumes

Iso-surfaces of zero U are generated to visualize the fore and aft recirculation regions in Fig. 20. The upstream surface is centered along the recirculation line of Fig. 10 and spreads in the spanwise direction as much as $1/4d$. In the near-wake, the surface takes on a shape similar to the U contours of the $3/2d$ downstream slice. A central 'crest' extends from nearly the trailing edge to about $2d$ downstream. Shoulder 'crests' develop with strong gradients near the trailing edge that dissipate quickly downstream. These 'crests' are most pronounced where the tertiary trailing system turns from an upstream to a

downstream orientation (where ω_x exiting the trailing edge entrains large amounts of fluid from near the plate). The spanwise spreading of this iso-surface extends the full width of the roughness element and curves along the entire trailing edge. Together these surfaces enclose a surprisingly large volume of upstream-directed flow near the roughness element. Fluid within the downstream recirculation volume follows paths similar to that of the secondary and tertiary vortex streamtraces. The fluid progresses slowly upstream towards the aft face of the element where it is lifted away from the surface and entrained by the top shear layer as it leaves the trailing edge.

MIPV is also used in Fig. 20 to contour a spanwise centered slice through the domain as well as the $3/2d$ downstream slice. The downstream slice indicates how intense the lateral influx of fluid is into the wake through the spanwise cradling high-speed regions. Due to symmetry of the simulation, $W = 0$ along the $z = 0$ slice so it is the magnitude of V that is displayed. A large region of upflow extends well into the freestream that is found as the boundary layer encounters the roughness element. Flow of the upper boundary layer then turns to a downward orientation back into the wake.
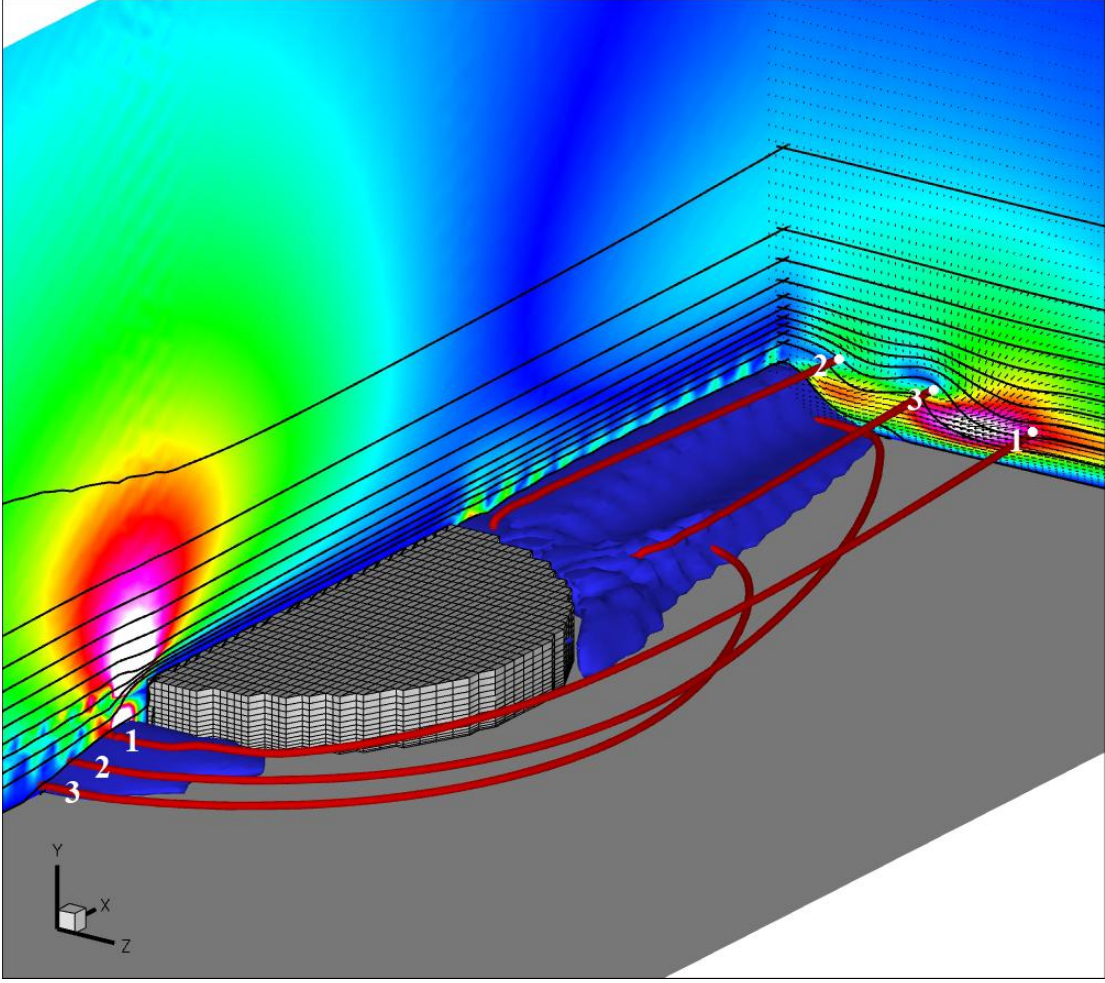
Fig. 20 Iso-surfaces of zero *U* and contour slices of *MIPV*. Lines are again 10% increments of U_∞. Small white dots mark where vortex streamtraces penetrate the downstream plane. Slight ripples in contours are Gibbs oscillations.

E. Parametric Flow Visualization

The above discussions allow us to understand the local flow structures about surface roughness with some confidence and in turn develop additional simulations. Of primary interest is the strong influence of roughness geometry on boundary layer receptivity. A set of simulations has been created that encompasses a range of Re_k and λ/d configurations (see Table 1), previously found to produce variations in transient growth.[12]

42

All simulations utilize the same domain and boundary layer initiation described in Chapter 2, Section C. Flow structures of these simulations are briefly presented here.

Table 1 Various parameters of parametric simulations.

Case	Re_k	d/λ	Re_d	k (mm)	d (mm)
1	216	1/3	4883	0.7304	6.35
2	166	2/5	5844	0.6416	7.60
3	166	1/3	4883	0.6416	6.35
4	166	1/4	3652	0.6416	4.75
5	127	1/3	4883	0.5582	6.35
6	48	1/3	4883	0.3414	6.35

Figure 21 displays the $3/2d$ downstream U contours previously described for all configurations. It can be seen that all cases maintain lateral gradients in the velocity deficit region. Each has three 'bumps,' spaced in the spanwise direction related to d/λ; the sharpness of gradients appears to correlate with Re_k. Clearly the projected area of the roughness element is directly related to how much of the boundary layer is hindered. Taller elements affect even upper regions of the boundary layer while the lowest amplitude cases barely disturb it. The widest configuration is found to perturb the boundary layer at spanwise stations far away from the centerline while the thinnest case only affects flow near the center.
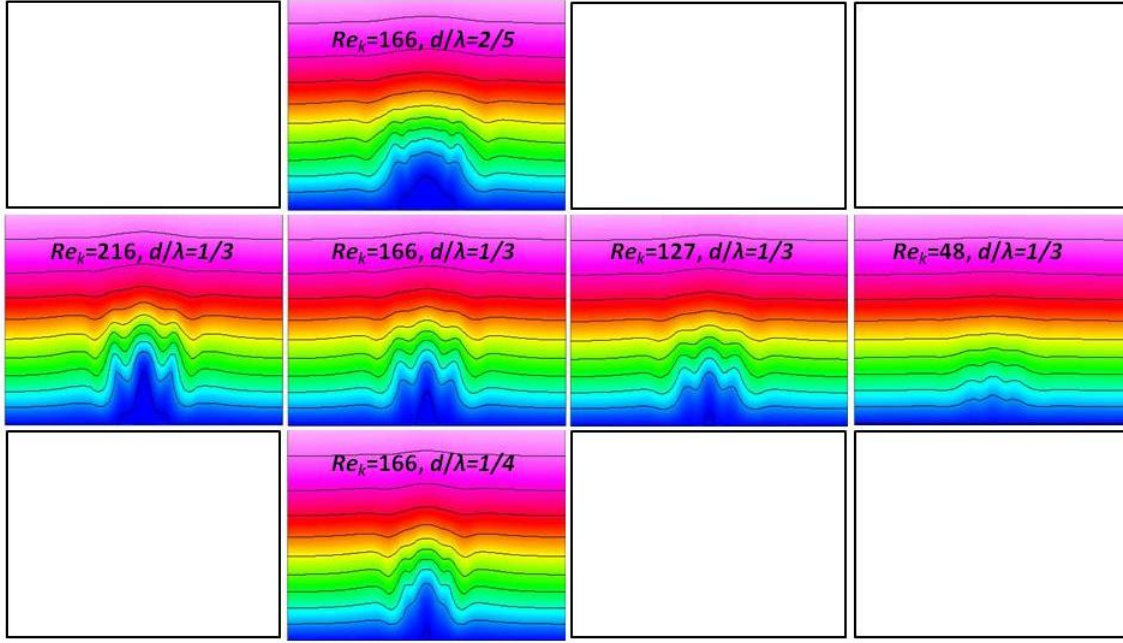
Fig. 21 Parametric study U contours $3/2d$ downstream. Lines are 10% increments of U_∞.

Upstream vortex topology is displayed in Fig. 22 again for all configurations of the parametric study. All profiles have fairly similar results except for the $Re_k = 48$ case which shows no upstream vorticies. In this case the lower boundary layer simply meets the element and flows over and around it without recirculating. Case 5 is also of interest as it is found to be a limiting Re_k for juncture flow topology. Here only two upstream vortex cores are found instead of three as predicted by Baker.[20] Given its Re_d Case 4 was expected to produce two upstream vortex cores but here displays an additional core very near the wall. This result will be discussed in more depth later. The three remaining cases produce the expected three vortex core topology described by Baker.
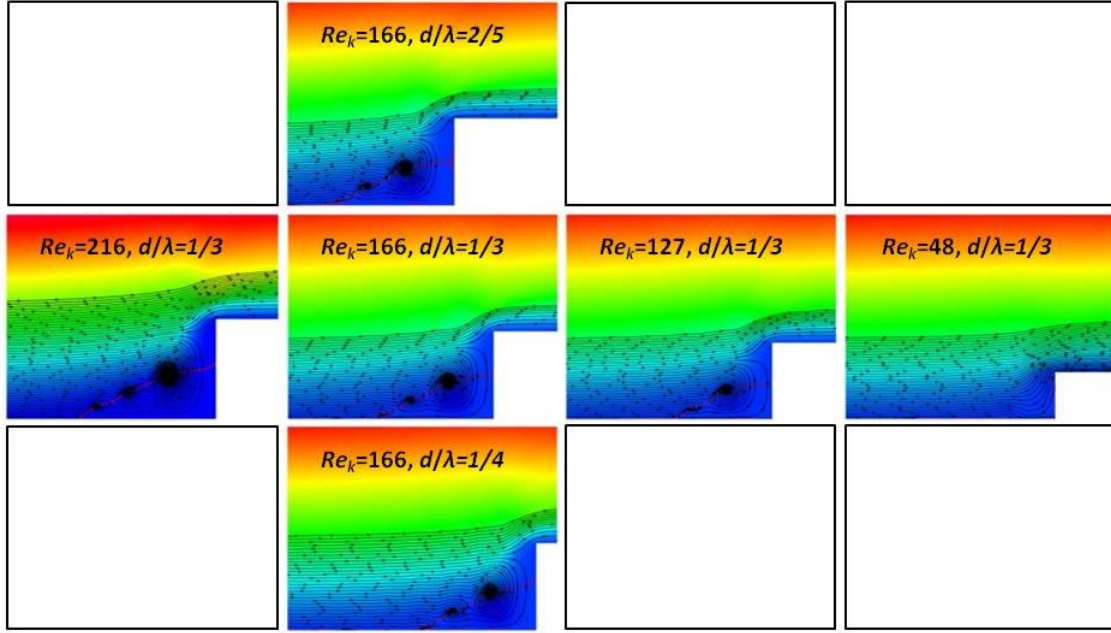
Fig. 22 Parametric study upstream vortex topology. Contours are of *U*, red line indicates recirculation line, and white rectangle notes the leading edge of the various roughness elements.

The near-field flow structures presented in Fig. 17 are replicated for each case and presented in Fig. 23. For most cases the results are similar showing divergence of the top shear layer that produces streamwise oriented vorticity within the velocity deficit region as well as lateral flow of the lower boundary layer as it flows around the roughness element. As expected the intensity of vorticity and velocity reduction downstream of the elements is dependent on the projected area.

It should be noted that the upstream vortex topology of the first four cases were shown to possess three vortex cores (see Fig. 22) although only Case 1 displays three vortex streamtraces. This is because when streamlines were placed at the upstream vortex singularity points for the other three cases only streamtraces of the strongest two vortex cores propagate downstream. The tertiary vortex core simply entrained the streamtraces and allowed them to drift into the immersed boundary simulating the flat plate. This is

45

due to the third vortex core's lack of strength and also its close proximity to the wall. Case 1 is shown in Fig. 22 with a third vortex core well away from the wall and with considerably more strength than cases with lower Re_k. It seems that the intensity, position, and therefore, number of upstream vortex cores found are dependent on the Re_k of the cylinder in question and not just on Re_d. This physically makes sense as the taller a cylinder is the more high-speed flow of the boundary layer it is able to capture in its upstream recirculation region.
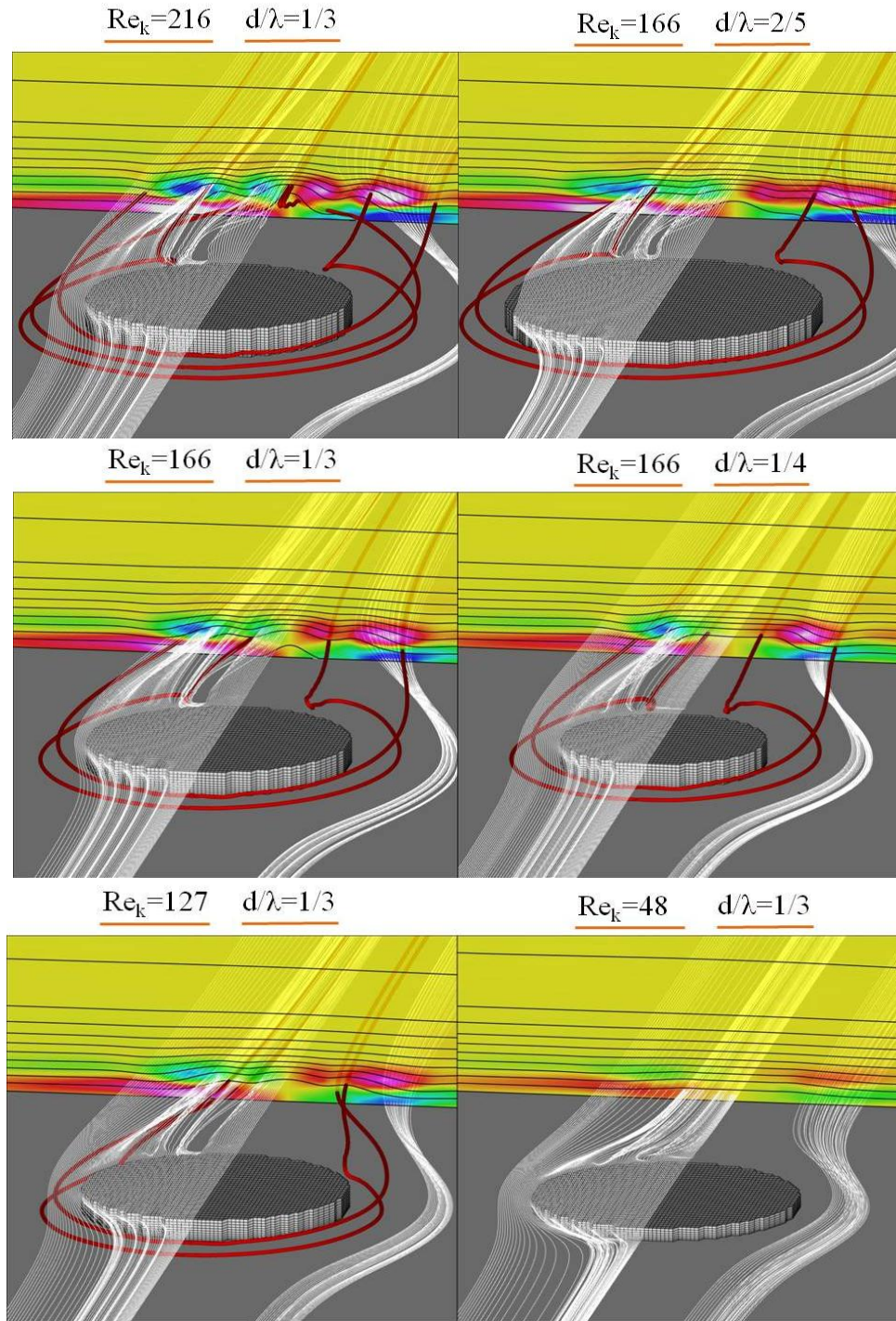
Fig. 23 Parametric study near-field flow structures. Downstream slice is contoured by ω_x and lined by 10% increments of U_∞. White lines and red tubes are streamlines. Configuration parameters are labeled above each figure.

Although we are able to describe the near-field flow structures of these simulations, the accuracy in modeling the experimental configurations is still in question. Of primary concern are the differences found between downstream 3/2*d* velocity contours of the experiments and simulations. The simple semi-triangular velocity deficit region measured in hotwire experiments has been presented in a number of studies over a range of geometrical configurations and therefore must be considered likely correct.[4,5,12,15,33,34]

Recent experiments at UT have utilized the LDA with a 4:1 beam expander that allows for measurement resolution superior to hotwire probes and the LDA measurements presented in Section IV.C. Preliminary results of these tests have shown velocity contours that are nearly identical to those presented by RV. The only variations seem to be a more complete representation of the cradling high-speed 'dips' and smoother curves of the velocity deficit region. No 'bump' structures are found, again suggesting a misrepresentation of the near-field by current DNS.

Filtering of the current DNS data sets (presented in Section IV.A) has proven to be very effective at eliminating the 'bump' structures of downstream velocity contours and, in turn, producing nearly identical results as hotwire experiments. As described in Sections V.A. and V.B. local high-speed flow within the velocity deficit region (the 'dips') is responsible for the lateral contour modes and stems from spanwise divergence of the top shear layer at the element trailing edge. This splitting has been shown to be related to the discreteness of the roughness element trailing edge and not the locations of streamtraces stemming from the upstream vortex cores (Section V.C). Therefore, proper modeling of the near-field requires eliminating or at least reducing the effects of modeling the roughness element with a crude cartesian mesh.

Three approaches are currently being investigated to resolve this issue. First, increasing the lateral Gaussian spread of the forcing field representing the roughness element may

reduce the stair step effect currently found. The extent of lateral spreading used for the simulations presented here has been kept consistent with prior studies using this DNS code. It seems, though, that this configuration of a cylindrical roughness element within the lower boundary layer may require a significant increase of the spreading parameter. The second approach involves increasing the simulation time step to more quickly reach later physical times. This involves reducing the forcing function gains θ and φ at some immersed boundary cells other than those representing the roughness element. Temporal stability of this DNS approach is currently dependent on these gains and not the CFL limit. The hope is that by advancing the physical flow time to much later periods, velocity contours may smooth in the same manner as the $Re_k = 166$, $d/\lambda = 1/4$ and $Re_k = 48$, $d/\lambda = 1/3$ cases that are found to completely lose their contour modes in Section VII.A. The final and most exhaustive approach is to increase spanwise and streamwise resolutions to more smoothly model the roughness element. This may yet be necessary.

Disturbance energy evolution presented in the next section is found to be consistent with prior experiments, suggesting that even though the near-field flow structure is not exactly represented, the current simulations accurately model transient growth produced by these roughness elements. The current transient growth theory filters flow parameters of the near-wake before reconstructing the downstream energy evolution. So, as previously stated, accurately simulating the disturbance wake downstream of roughly $4d$ is the most critical consideration for theoretical analysis. Also, the contour modes present in the near-wake of current results are of a much higher spanwise spatial frequency than the primary energy modes and as such will dissipate quickly downstream. This is clearly seen in the $6d$ velocity contour of Fig. 8 which maintains very little of the $3/2d$ lateral gradients. Therefore, the simulations presented here are useful for the development of transient growth theory even the though the near-field possesses discrepancies with respect to the experimental configurations modeled.

49

VI. DISTURBANCE ENERGY EVOLUTION

Downstream disturbance energy of the six configurations simulated is now presented under the assumption that the final iterations have reached a reasonably steady state. Fairly different disturbance energy characteristics are found between the various geometrical setups. The disturbance energy evolution of the fundamental spanwise wavelength λ_k, and its first three harmonics, $\lambda_k/2$, $\lambda_k/3$, and $\lambda_k/4$ are of primary interest as these modes hold a majority of the downstream energy. Qualitative agreement is found with the WRE experiments[12] for nearly all modes in every configuration presented. Total disturbance energy E_{rms} is also used to better quantify results with respect to experiments.

A. Total Disturbance Energy

To begin this quantitative analysis the boundary layer scale δ is computed midway between the roughness elements where the flow is assumed to be largely unaffected. The wall normal direction and velocities are normalized by δ and U_∞, respectively, to appropriately compare with experiments. Next the disturbance velocity U' is used to calculate the spatial root-mean-square disturbance velocity,

$$U'_{rms}(x,\eta) = \sqrt{\frac{1}{N_z}\sum_{k=0}^{N_z} U'^2(x,\eta,z)}\,, \tag{4}$$

throughout the downstream domain. This disturbance profile squared is representative of the total disturbance energy of our simulations,

$$E_{rms}(x) = \int_0^\infty U'_{rms}(x,\eta)^2 d\eta\,. \tag{5}$$

The downstream evolution of this quantity is the most useful for comparing with experiments and validating our simulations.

Denissen and White[33] (DW) presented new experimental results of a $Re_k = 202$, $d/\lambda = 1/3$ case alongside additional subcritical roughness experiments.[5,12,15,33] These data sets were scaled by Re_k^2 and found to collapse very well to two separate profiles (see Fig. 24). DW

50

noted the variation between profiles as a discrepancy of δ calculated for either set of experiments. The experiment of EW[15] we are concerned with falls into the red band while a number of the experiments of WRE[12] fall into the blue band of data.
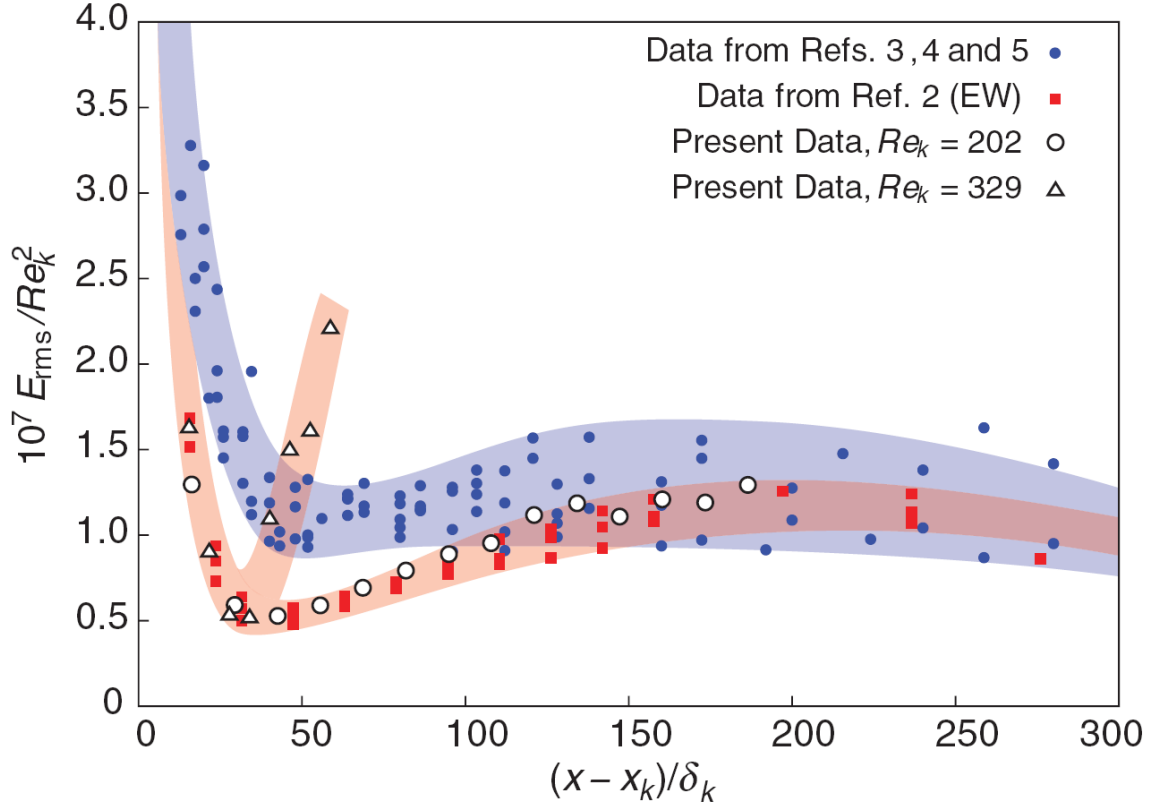

Fig. 24 Scaled total energy presented in DW.[33] Experiments corresponding to the DNS parametric study are found in both profiles.

Figure 25 displays the scaled total disturbance energy evolution downstream of the simulated roughness elements along with three corresponding experiments of WRE (Re_k = 254, Re_k = 195, and Re_k = 143 with d/λ = 1/3 in all cases). All configurations produce similar profiles consisting of a sharp energy decline immediately downstream of the elements, a region of geometry dependent transient growth, and an eventual energy decay. Of specific note is that the regions of strong energy decay found shortly downstream (($x - x_k$)/δ < 45) of the roughness elements are representative of the non-linear region neglected by current transient growth theory.[14] Minimums of the various

51

profiles occur at roughly $4d$ downstream of the elements, giving way to transient growth that is predictable by linear stability theory.

A number of the simulation energy profiles are consistent with experimental findings yet some vary significantly. Total energy evolution of the three largest elements of the Re_k series (cases 1, 3, and 5) collapse fairly well to one another and with the experiments presented. Energy minima are nearly identical and the transient growth downstream varies directly with Re_k. The shortest roughness element (case 6) does not correspond quite as well. Its energy minimum is far less than the remaining Re_k series elements' and is found further downstream. Transient growth of case 6 occurs much like others of the Re_k series and would likely converge with their profiles in a similar fashion had the minima matched.

This scaling of E_{rms} by $Re_k{}^2$ is not very helpful for the d/λ series as can be seen by the large variation amongst the three corresponding energy profiles (cases 2, 3, and 4). These three cases produce similar energy minima at matching downstream locations although the amplitudes do not converge quite as well as those of the Re_k series. The range of transient growth produced by these elements is wide spread. Both growth rates and energy peaks are found directly related to element size, as expected from the d/λ series of WRE.[12] However, energy evolutions like this have not been similarly presented with varying d/λ configurations. It is unclear whether or not a scaling similar to the squared Re_k is available for the d/λ series or if both sets could be completely collapsed together.
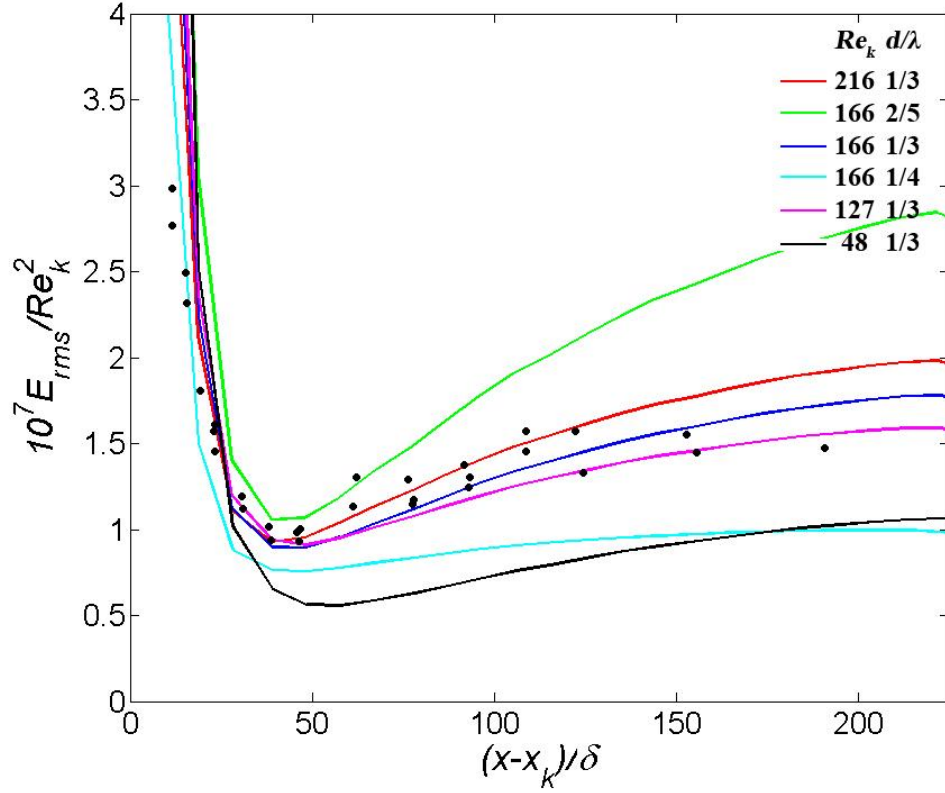
Fig. 25 **Scaled total disturbance energy evolution. Lines are current simulations colored by configuration and markers are three experimental cases from WRE.[12]**

B. Energy Components

The purpose of using distributed roughness elements is to specifically excite spanwise energy modes. Configurations that directly input integer wavelengths have been found to produce a significant amount of transient growth within that specific energy mode. Therefore, the configurations used in this study are such as to generate disturbance energy of the 1/3 and 1/4 wavelengths. The $d/\lambda = 2/5$ configuration will be shown to disperse its energy to integer modes greater than and less than its input wavelength.

An analysis approach was developed by Rice[33] to represent spanwise energy modes of the downstream disturbance wake. To begin, a Fourier transform is taken of U' in the full

spanwise domain at all x and y stations. Coefficients of these transforms are used to develop the power spectral density *PSD* of the signal. The power associated with each wavelength component is drawn from this analysis. Values are computed at each downstream station as such:

$$PSD_m(\eta) = \frac{2}{N_z^2}\hat{U}_m(\eta)^2 \qquad \text{for } m = 1,2,\ldots (\tfrac{N_z}{2}-1).$$ (6)

A modified analog to Parseval's theorem states that the total energy of the original signal is not modified by transforming to Fourier space and thus,

$$\left[U'_{rms}(\eta)\right]^2 = \sum_{m=0}^{N_z} PSD_m(\eta).$$ (7)

Therefore, we can be sure that the disturbance energy contained in any particular mode will be scaled accordingly with the total disturbance energy. Finally, the total energy, energy modes, and *PSD*'s are related as:

$$E_{\lambda/m} = \int_0^\infty PSD_m(\eta)d\eta,$$ (8)

$$E_{rms} = \sum_{m=0}^{N_z} E_{\lambda/m}.$$ (9)

Figure 26 displays experimental energy evolution of various modes for both the Re_k and d/λ series.[12] Simulations of the present parametric study are presented in a similar manner in Figs. 27-30. Variation between energy magnitudes of the experimental results and current simulations are thought to be associated with the different spanwise grids used for analysis. Fewer data points are collected across λ in the experiments and as such the Fourier coefficients produced by this reduced signal must each hold more of the total energy. Total energy of the DNS domains is comparable to that of the experiments and, as Eq. 9 states, the sum of the individual energy modes must equal the total disturbance energy. Therefore, the fewer modes present in the experimental signal must individually

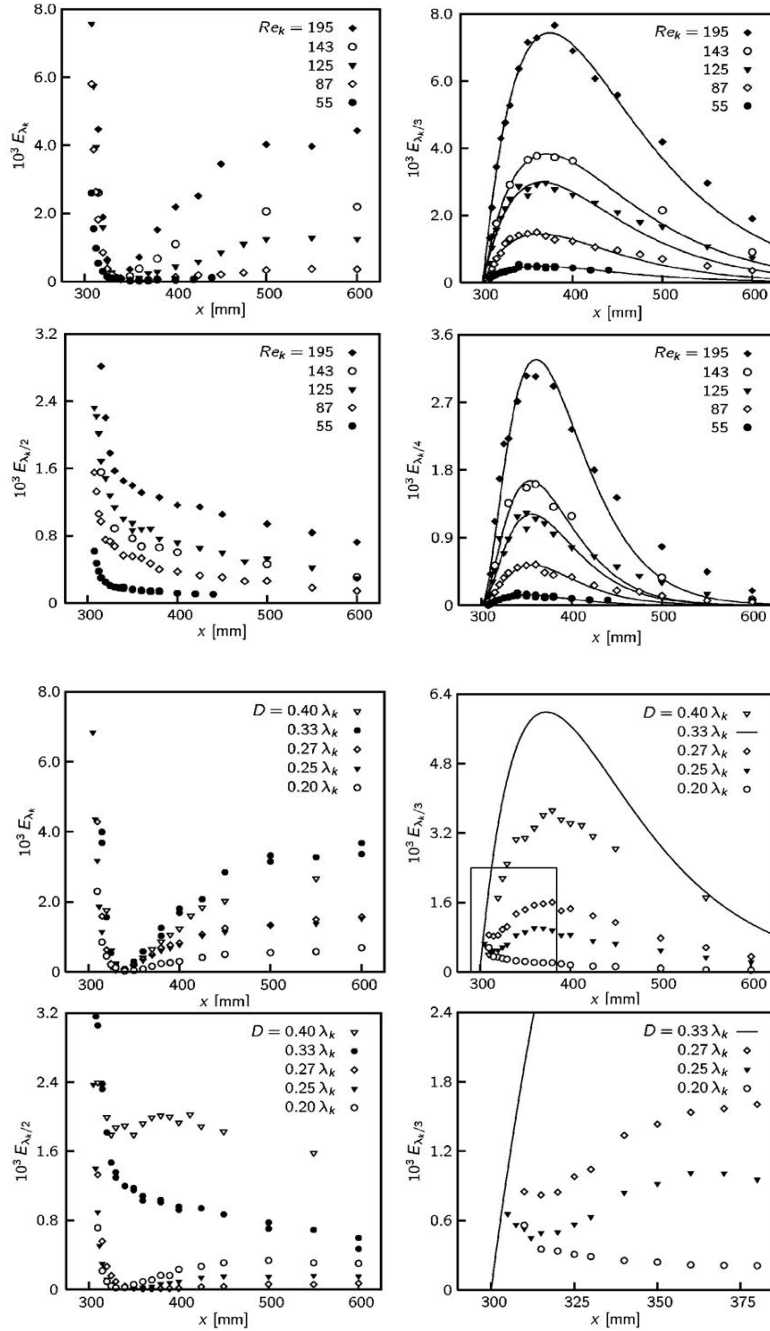hold more energy to account for the lack of high frequency modes which are only present in the DNS signal.

Fig. 26 **Experimental energy evolution of the primary harmonics for the Re_k series (top four figures) and the d/λ series (bottom four figures). Taken from WRE.[12]**

Energy evolution of the primary harmonics is now presented for all configurations simulated. Disturbance energy of the fundamental wavelength is very high immediately downstream of the roughness elements but quickly decreases to negligible values at $(x - x_k)/\delta = 45$ (see Fig. 27). Minima of E_λ are found at nearly the same station for all configurations, after which transient growth occurs in varying degrees. Just before the downstream extent of the domain used for simulations is reached energy decay begins. Energy growth of this mode beyond the downstream minimum has been described as qualitatively similar to that of optimal disturbances.[34] The magnitude of disturbance energy is found to be directly related to the projected area hindered by the roughness element in question. Experiments do not agree with this last finding as the $d/\lambda = 2/5$ configuration of WRE produces slightly less energy than its $d/\lambda = 1/3$ counterpart throughout the domain. All other DNS configurations are found to possess approximately half the energy of corresponding experiments.[12]
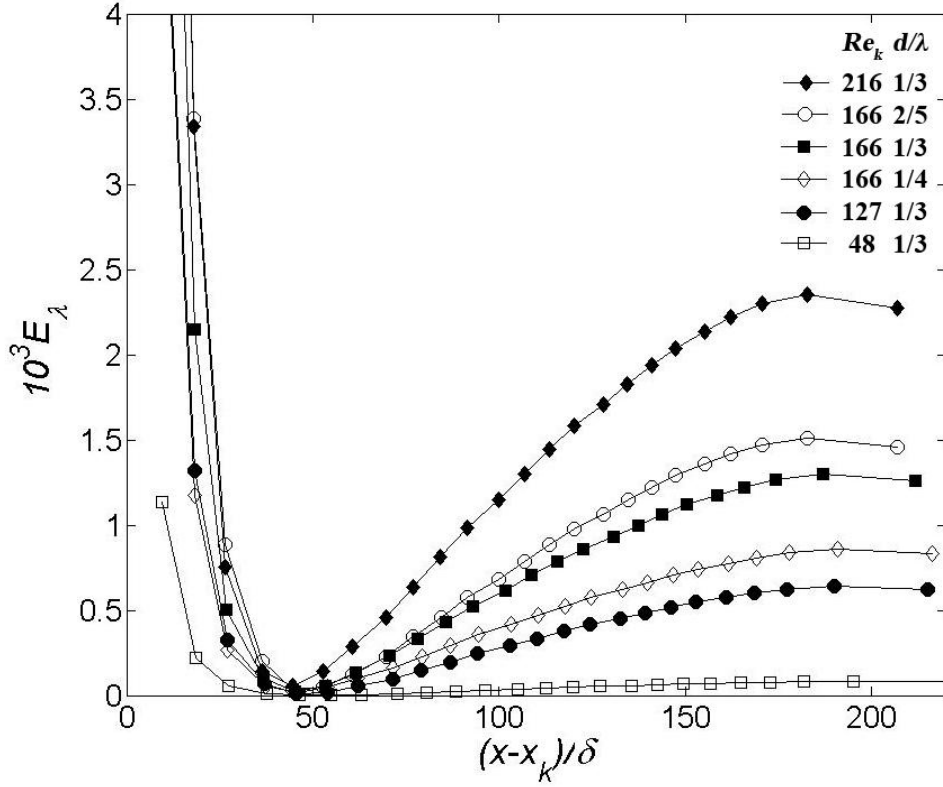
Fig. 27 The λ component of disturbance energy.

In general, the $E_{\lambda/2}$ evolution has been found to consist of simply monotonic decay for d/λ = 1/3 configurations while variations of this parameter may display different profiles.[12] Simulations of the Re_k series agree with this trend of monotonic decay except for the largest amplitude case where a very slight increase of energy is found downstream of the near-wake decay (see Fig. 28). There is no deviation from this trend in experiments so it is assumed that this is likely an effect of the simulation's relaxation.

Alternate d/λ configurations affect the $E_{\lambda/2}$ evolution as seen in the Re_k = 166, d/λ = 1/4 case which produces very low energy throughout the domain. Decay in the roughness element near-wake leads to almost negligible energy downstream that is on the order of

57

that of the Re_k = 48 setup. Experiments find a small amount of energy growth for the d/λ = 1/4 configuration, although it is minimal and the difference in magnitudes with respect to the standard case (Re_k = 166, d/λ = 1/3) is comparable to that of DNS results. On the other hand, the Re_k = 166, d/λ = 2/5 case is approaching a direct input of the λ = 1/2 wavelength and therefore shows significant energy growth after an initial period of decay. This profile is very similar to its experimental counterpart though energy magnitudes are again approximately half that of the experiments.[12]
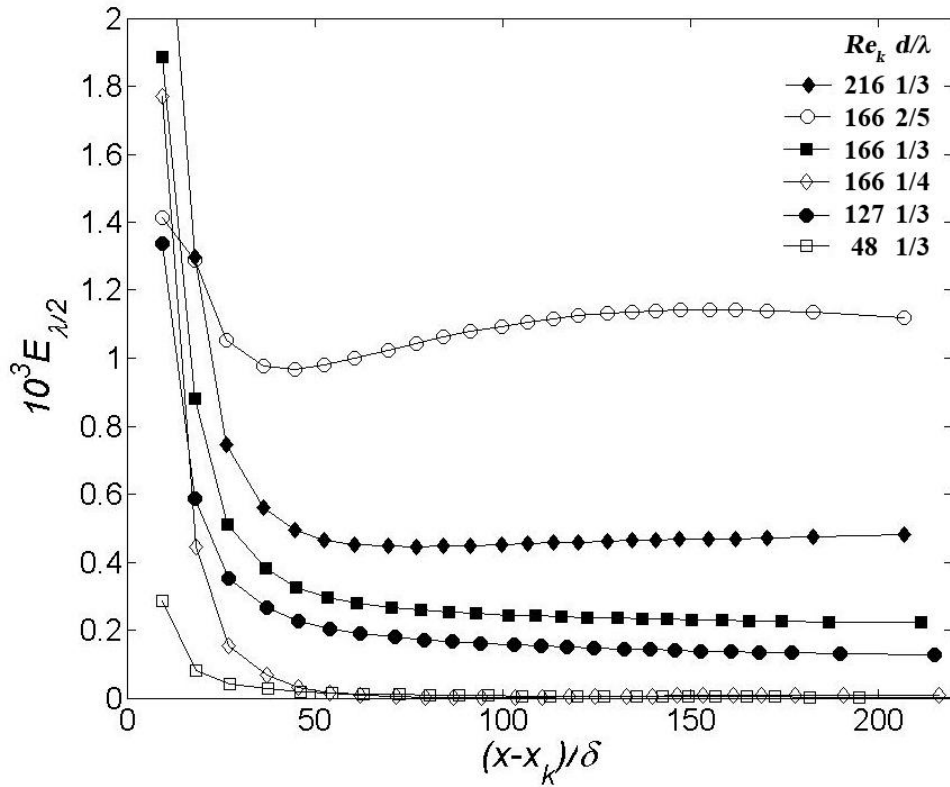

Fig. 28 The λ/2 component of disturbance energy.

The importance of Re_k to transient growth can be clearly seen in the $E_{\lambda/3}$ evolution of Fig. 29. Variation of the energy maxima is quite large between all four configurations that directly input the λ = 1/3 wavelength. Dependence on Re_k has been well examined for this

58

d/λ, so much so that it is commonly the primary energy mode used to display transient growth. This energy evolution has been characterized in WRE as a linear energy growth followed by exponential decay regardless of the roughness amplitude.[12] Peaks of the $E_{\lambda/3}$ profiles are approximately three times less than those of experiments.

Energy growth and decay of the $Re_k = 166$, $d/\lambda = 2/5$ case is found to also follow the standard profile for this energy mode. Unlike experiments, though, the magnitudes are significantly higher than the $Re_k = 166$, $d/\lambda = 1/3$ case. This result makes physical sense as the $d/\lambda = 2/5$ configuration falls between the $\lambda/2$ and $\lambda/3$ wavelengths. So, much like in the $E_{\lambda/2}$ evolution, large amounts of disturbance energy are accumulated in the $\lambda/3$ component.

The short wavelength case ($Re_k = 166$, $d/\lambda = 1/4$) presents another variation of the $E_{\lambda/3}$ evolution. As with experiments, weaker disturbance energy is found with respect to a majority of the larger wavelength cases as well as a slightly different profile. Transient growth is not found immediately downstream of the roughness element. Instead, a reduction of energy in the near-wake gives way to weak transient growth further downstream. After which, exponential decay of the reduced energy peak is found.
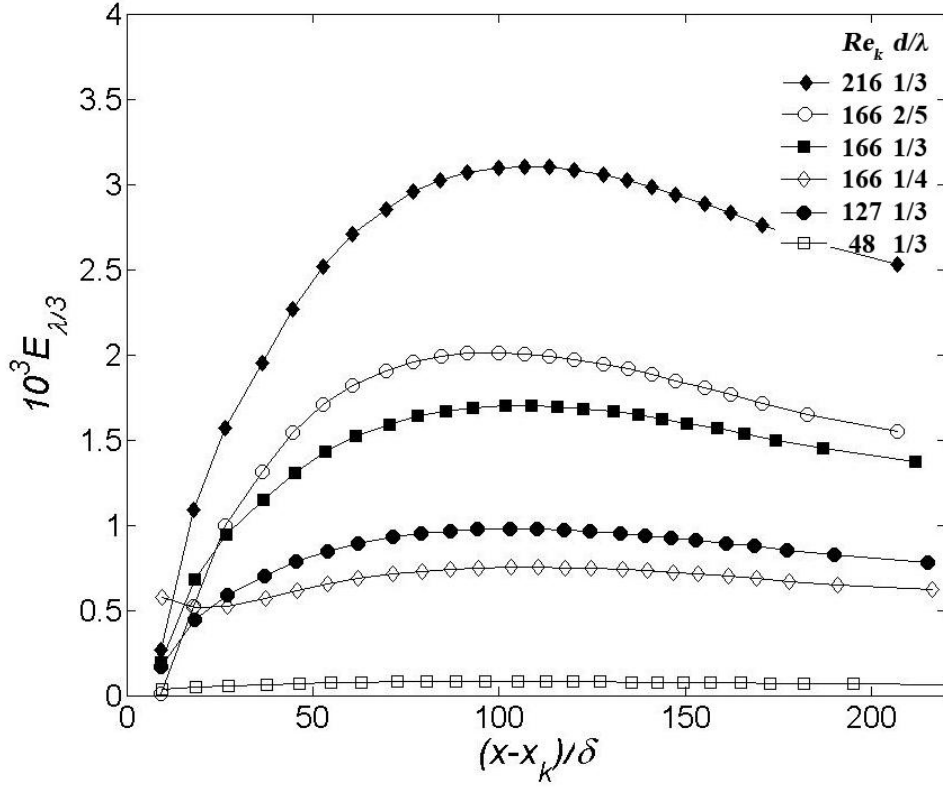
Fig. 29 The $\lambda/3$ component of disturbance energy.

Results similar to the $E_{\lambda/3}$ profiles of Fig. 29 are found in the $E_{\lambda/4}$ evolution of Fig. 30. WRE again described energy evolution of the Re_k series as having transient growth (quadratic with respect to downstream distance) to maxima that are highly dependent on Re_k, followed by exponential decay. On the other hand, energy dependence on the configuration input wavelength has inverted for this mode as the $d/\lambda = 1/4$ case is now directly exciting the $\lambda/4$ energy component and the $d/\lambda = 2/5$ case produces little energy. The largest wavelength configuration maintains a very small amplitude profile similar to the $d/\lambda = 1/4$ case's $E_{\lambda/3}$ evolution. Profiles again have magnitudes roughly a third that of the corresponding experiments.
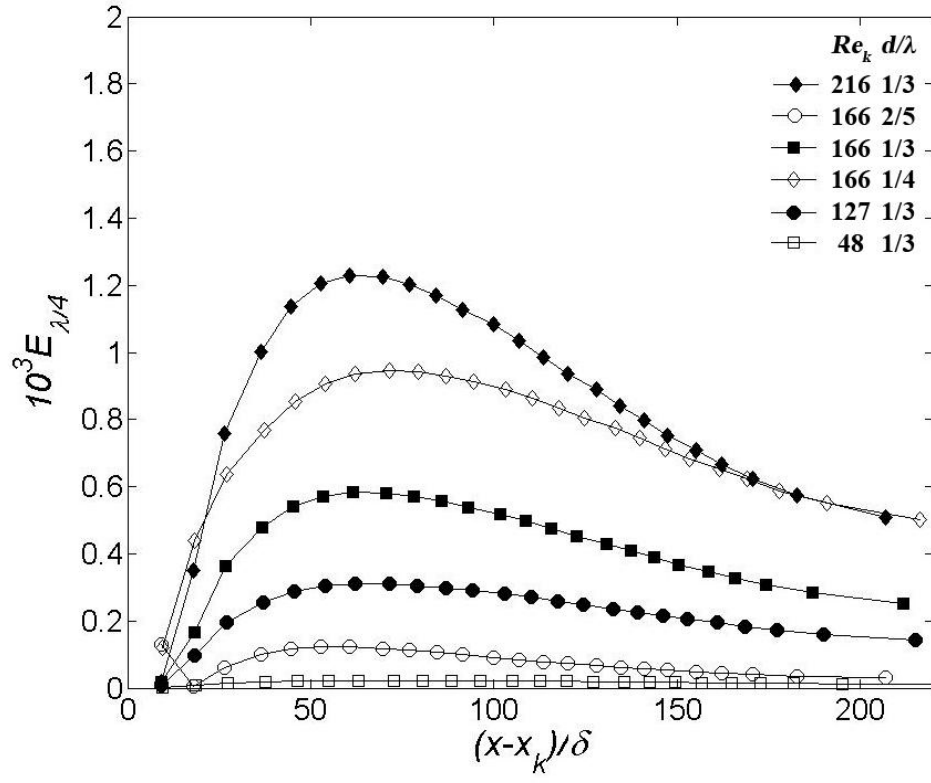
60

Fig. 30 The λ/4 component of disturbance energy.

VII. TIME VARIANCE OF SIMULATIONS

The cases presented here are all consistent with gradual large time scale variations, perhaps due to the unphysical initiation of the roughness elements and the physically slow development of the disturbance wakes. Early stages of these simulations produce a variety of flow structures likely not found in the experiments they model. Instantaneous initiation of forcing is used to introduce the elements into the domain. This triggers a region of turbulence that propagates downstream until reaching the buffer zone, where it is quickly eliminated. Flow near the roughness element relaminarizes shortly after the turbulent region is generated, although it is not yet representative of a steady state experimental configuration. A gradual period of reorganization is found around the element as the incoming laminar boundary layer introduces steady fluid into the near-field. Experiments allow the flow field to develop over an array of fixed elements for an extended period of time before collecting data to avoid variations such as this. The transient period in our simulations is found to be highly dependent upon roughness geometry. Larger Re_k and d/λ configurations produce much greater variation during relaxation than their smaller counterparts. After this period, the upstream recirculation region has developed its vortex topology and flow structures of the near-wake begin to settle. A survey of the near-field now displays fairly time-independent flow about the roughness element, consistent with the expected result but, a closer look shows otherwise.

A. Velocity Contours

Downstream U contours (see Fig. 31) led to a majority of the thesis presented in this work and have since shown the greatly underestimated relaxation time needed to accurately model this flowfield. Further iterations are simulated after the near-field has reached a seemingly constant state and the U contours are captured. A very slow relaxation is found as the plots shift ever so slightly over large periods of time. At first

lateral gradients appear to be increasing but, after many steps they are found to subside. Time variance is strongly dependent upon the roughness geometry and as such, full reduction of these gradients is only found in the smallest configurations, although it is expected to eventually occur in all cases.
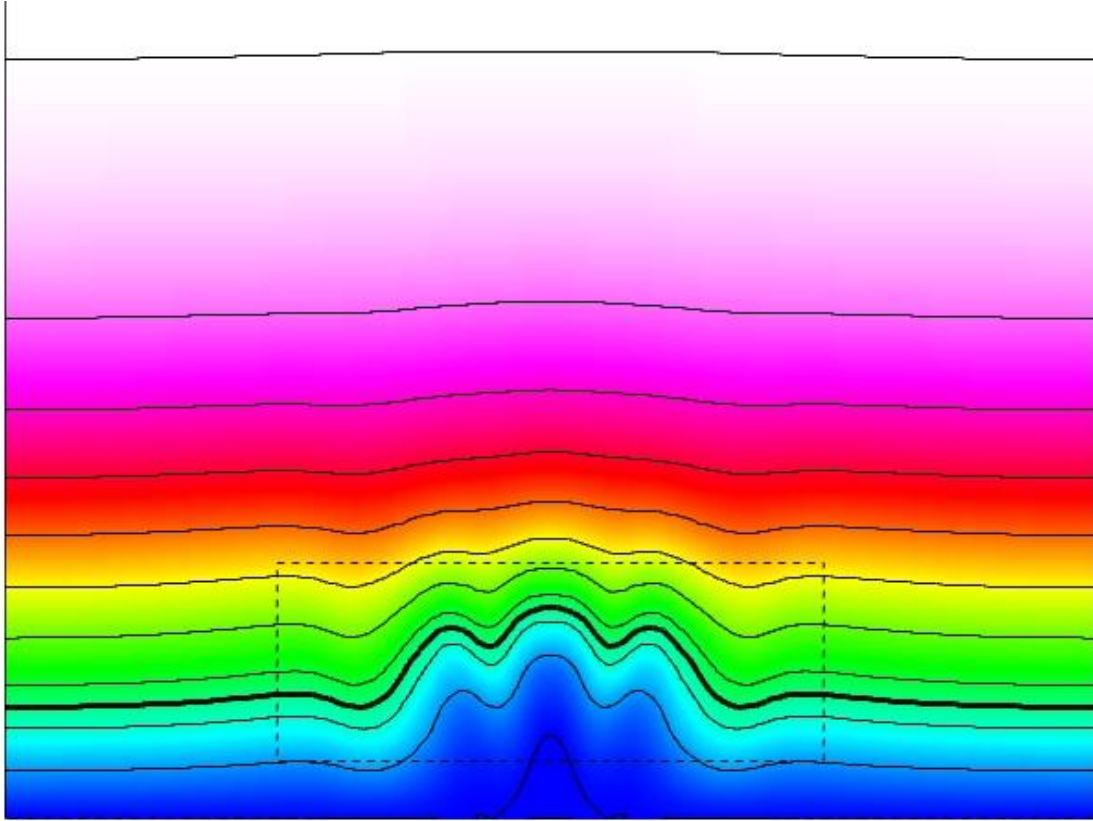

Fig. 31 Instantaneous U contour at approximately 3/2d downstream of the Re_k = 166, d/λ = 1/3 roughness element. Thin lines are 10% increments of U_∞. The thick line is the 1/4U_∞ contour and the dotted box represents the domain to be further used. Figure is stretched about four times in y.

Figure 32 displays the late stage relaxation of 1/4U_∞ contours (discussed in Fig. 31) for the range of configurations. Each set of contours spans the final 60,000 iterations (of the 150,000 total) and is stretched 10 times in the wall normal direction to emphasize variation. A significant amount of variation is found for each configuration. Lateral

gradients are continually decreasing in time, suggesting that no case can be confidently described as fully relaxed.

Geometry dependence is visible in the contours themselves as well as in the time variation. Larger values of Re_k and d/λ produce greater velocity deficits in the wall normal and spanwise directions, respectively. Gradients in the wake of larger roughness elements seem to decrease more slowly in time than their smaller counterparts as noted by the center 'crest' of these contour sets showing negligible change in time. The consistent three 'bump' shape has reduced completely for the smallest element of each series (cases 4 and 6). Although both of these cases have lost their contour modes, the variation seems as if it may continue indefinitely.

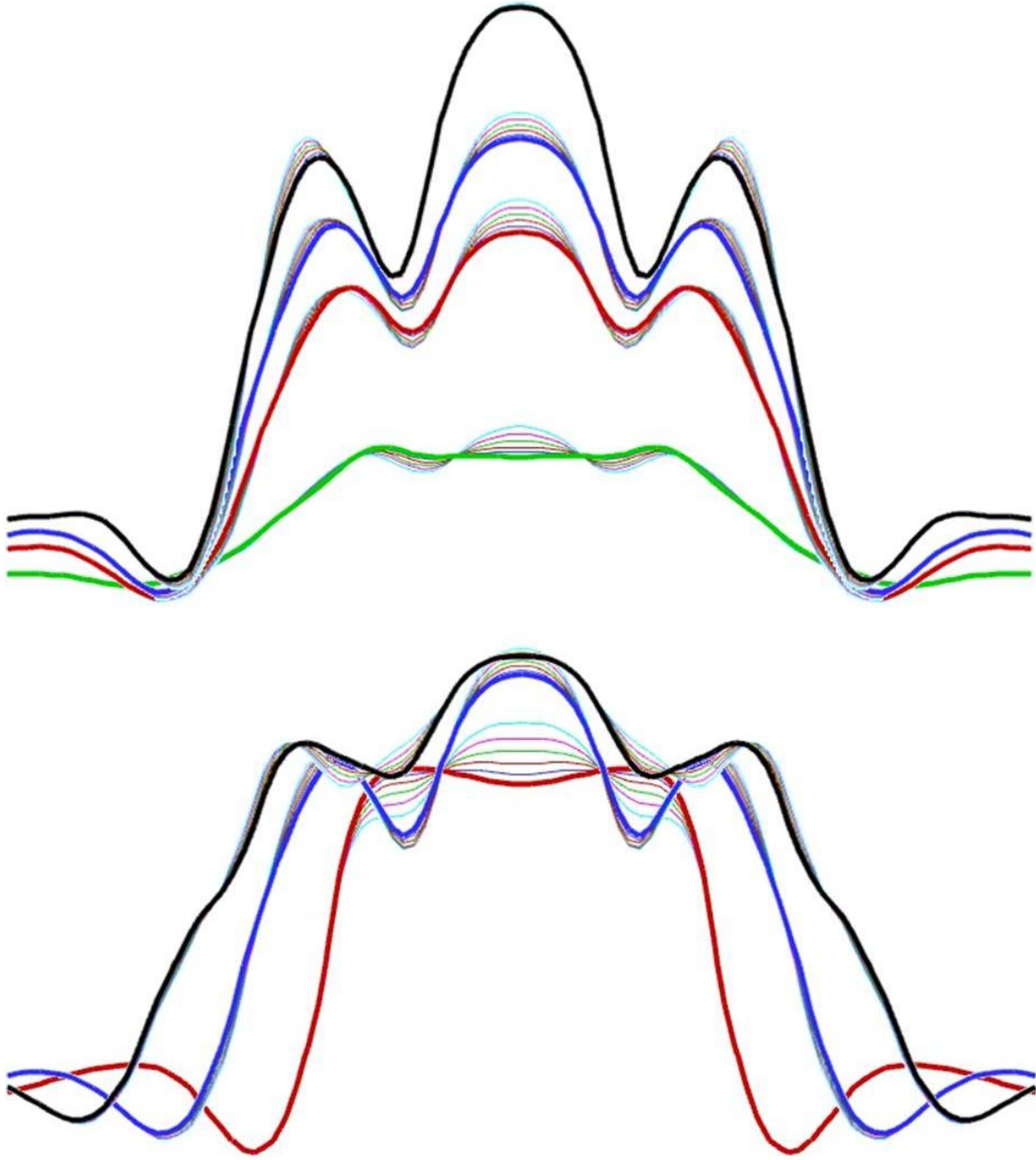**Fig. 32** Time variance of the $1/4U_\infty$ contours. The top is the Re_k series and the bottom is the d/λ series. Thin lines span 60,000 iterations prior to the presented data sets (thick lines). Figures are stretched 10 times in y.

B. Energy Evolution

This extensive relaxation time is not restricted to the near-field where non-linearities are expected; downstream disturbance energy is also found to be affected by this long time scale. Figure 33 displays the time varying disturbance energy spectrum for the $Re_k = 166$, $d/\lambda = 1/3$ case. The time frame shown is identical to that of Fig. 32.

Relaxation is found to be present throughout the entire downstream domain. Significant variation occurs in all disturbance energy modes presented with the largest change in time occurring in the $E_{\lambda/3}$ evolution. This is understandable due to the $d/\lambda = 1/3$ configuration used to specifically excite that spanwise wavenumber. Other configurations simulated are consistent with this finding as the energy mode corresponding to their d/λ configuration always displays the largest variation in time. Time variability also occurs in the total disturbance energy profile indicating that relaxation of the energy profiles may be due to a redistribution of energy between the individual modes over long periods of time.
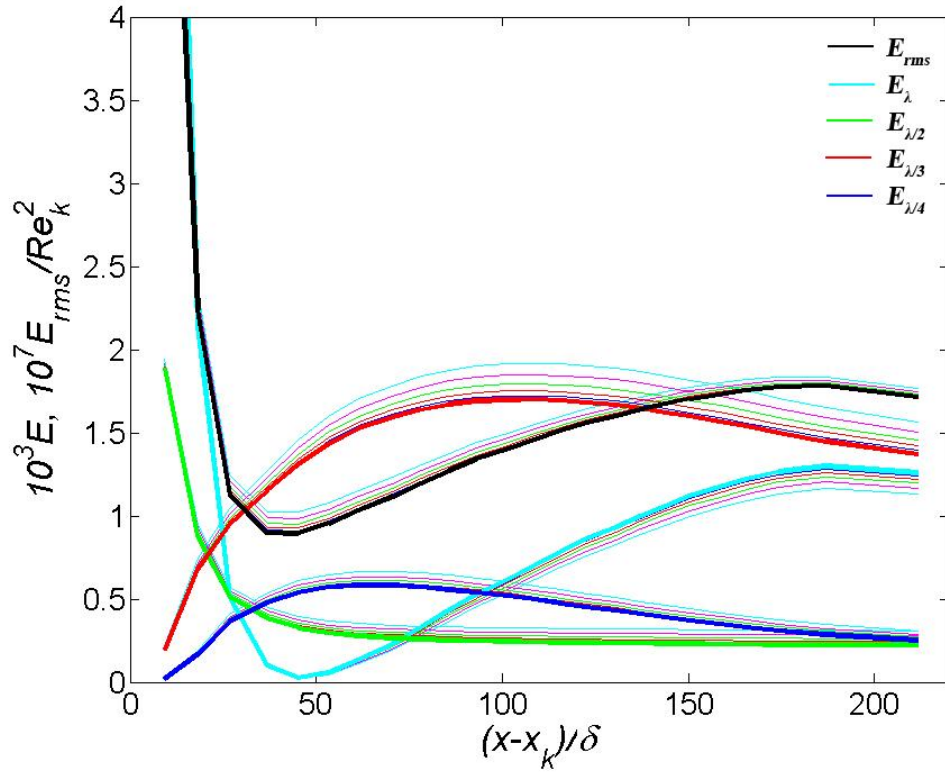
Fig. 33 **Time varying disturbance energy spectrum. Thin lines span 60,000 iterations prior to the presented data set (thick lines).**

Variation of the energy mode magnitudes with respect to experiments may be an additional side effect of the simulation relaxation process. As seen in Fig. 32 the downstream wake maintains spanwise modality of its *U* contours. These gradients have a high spatial frequency relative to the primary wavelengths used for energy analysis. It is likely then, that the simulations possess more disturbance energy in higher spatial frequencies than is physically present in steady state experiments and need to further relax. This would in turn reduce the energy within the first four harmonics, skewing their profiles.

C. Steady State Estimates

By tracking the total downstream disturbance energy, E_{rms}, we are able to estimate when these simulations may reach a steady state. The energy of Fig. 25 is integrated throughout the entire downstream domain,

$$E = \int_{x_k}^{x=450} E_{rms}(x)dx, \tag{10}$$

at time steps displayed in Figs. 32 and 33. An exponential decay function is fitted to the energy differences in time and used to predict when the various configurations are likely to relax. A maximum energy difference of 0.001 is arbitrarily selected as the criterion for acceptable relaxation.

The smallest roughness configuration (Re_k = 48, d/λ = 1/3) is found to already be sufficiently relaxed. This was expected due to the minimal contour variation displayed in Fig. 32, the very low E_{rms} values calculated, and the ability of the BES reconstruction (Section I.B) performed at Texas A&M to easily predict the downstream energy evolution (see Fig. 34). Two similar cases (Re_k = 127, d/λ = 1/3 and Re_k = 166, d/λ = 1/3) are expected to reach a steady state within 100,000 additional iterations (almost twice the presented total). Simulations are underway that may allow an increased time step to be used which would greatly reduce the number of additional iterations required.
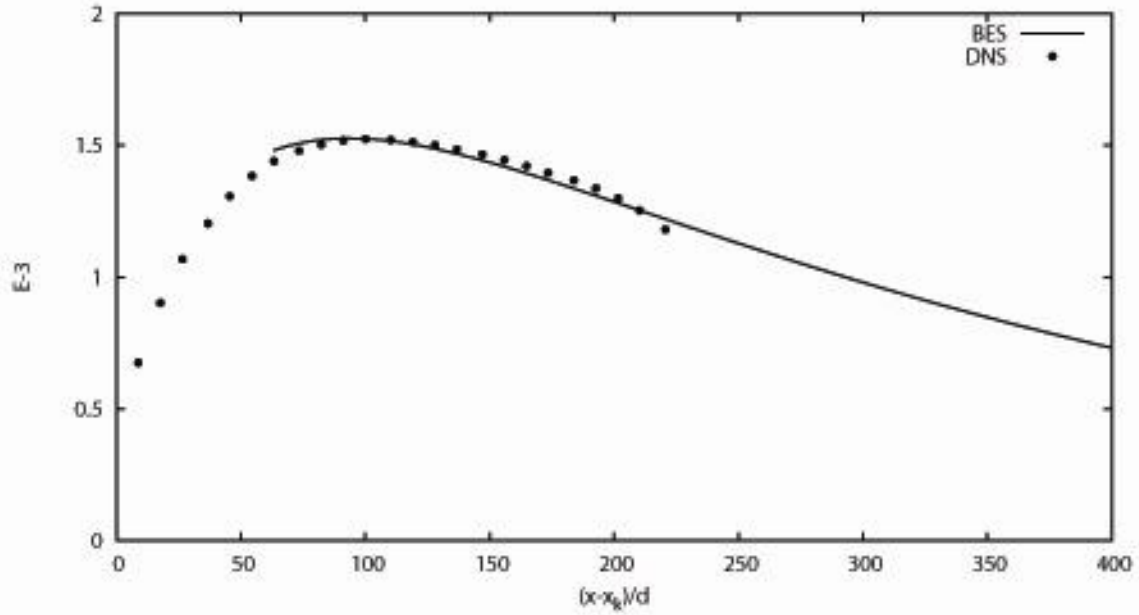
Fig. 34 BES reconstruction of the third energy mode for the $Re_k = 48$, $d/\lambda = 1/3$ simulation.

It was expected that the thinnest roughness element ($Re_k = 166$, $d/\lambda = 1/4$) would reach a steady state quickly due to its relatively small downstream recirculation region. To the contrary, though, it is found to require nearly three times the additional run-time as its accompanying $d/\lambda = 1/3$ configuration. The largest two roughness elements used ($Re_k = 216$, $d/\lambda = 1/3$ and $Re_k = 166$, $d/\lambda = 2/5$) are interesting as well as they have yet to produce a consistent exponential decay of energy difference in time. These odd findings make it difficult to relate relaxation time to the geometrical parameters of this study.

Useful insight may still be gathered from these simulations, even if they have not reached a steady state. As mentioned previously, a macroscopic view of even the near-field shows little change when standard visualization is employed. Therefore, flow structures about the roughness elements are likely closely representative of the physical configurations modeled. The energy component evolutions of Fig. 33 display results consistent with prior transient growth studies and should be useful for theoretical analysis.

69

VIII. CONCLUSIONS

Flow structures in the near-field of a subcritical cylindrical surface roughness element are modeled via direct numerical simulation. The case presented is representative of hotwire measurements taken downstream of a periodic array of $Re_k = 202$, $d/\lambda = 1/3$ roughness elements in a flat plate boundary layer.[15] Prior simulations have shown discrepancies between one another as well as with experimental results.[16,17] The primary focus of the current work is resolving these issues as well as the generation of a data set useful for transient growth theoretical analysis.

Current results are compared directly with the former studies and found to differ in some of the flow details. Near-wake U contours display 'bump' structures similar to those of SG, as opposed to the smooth velocity deficits presented by RV and EW. Similar upstream vortex topology is found between current DNS and SG while the simulation of RV differs.

Interpolation of current results onto the *experimental* mesh reduces the lateral gradients captured by DNS in downstream U contours and produces excellent agreement with the results of EW. Laser doppler anemometry experiments are performed that also cannot identify 'bump' structures due to a spanwise resolution similar to the hotwire probe of EW. The upstream vortex topology of current DNS coincides with previous juncture flow experiments[20] and is indirectly verified by flow visualization experiments in water.

Visualization of local flow structures is utilized to characterize the roughness element near-field. Downstream slices show ω_x moving high-speed flow into the velocity deficit region, creating the 'dip' structures of the present results. Regions of high ω_x are found to stem from the top shear layer where spanwise vorticity is redirected as flow leaves the element's trailing edge. Vorticity generated at the wall as the lower boundary layer flows

70

around the element has been shown to diffuse into and largely eliminate vorticity propagating from the upstream recirculation region. Streamlines shown in flow visualization experiments likely do not possess any significant vorticity and therefore would not affect the downstream flow structure. Alternating high and low-speed streaks downstream of surface roughness are therefore due to ω_x generated by the top shear layer and not horseshoe systems.

Disturbance energy evolution has been shown to be fairly consistent with experimental findings. Quantitative results of E_{rms} are within a reasonable range of prior experiments, pointing to the simulation's ability to reasonably model the physical flow field. The difference in spanwise resolution of experiments and DNS is likely too great to expect similar magnitudes of the primary integer energy modes, although, consistent trends are captured for all configurations. Nevertheless, full temporal relaxation of the simulations will need to be reached before expecting accurate results. Calculations have indicated that steady state solutions of even the most realizable configurations may require nearly twice the current number of iterations.

REFERENCES

[1]Ellingsen, T. and Palm, E., "Stability of Linear Flow," *Physics of Fluids*, Vol. 18, No. 5, Apr. 1975, pp. 487-488.

[2]Landahl, M.T., "A Note on an Algebraic Instability of Inviscid Parallel Shear Flows," *Journal of Fluid Mechanics*, Vol. 98, May 1980, pp. 243-251.

[3]Reshotko, E. and Leventhal, L., "Preliminary Experimental Study of Disturbances in a Laminar Boundary Layer Due to Distributed Roughness," AIAA Paper 81-1224, Jun. 1981.

[4]White, E. B., "Transient Growth of Stationary Disturbances in a Flat Plate Boundary Layer," *Physics of Fluids*, Vol. 14, No. 12, Dec. 2002, pp. 4429-4439.

[5]White, E. B. and Ergin, F. G., "Receptivity and Transient Growth of Roughness-Induced Disturbances," AIAA Paper 2003-4243, Jun. 2003.

[6]Reshotko, E., "Transient Growth: A Factor in Bypass Transition," *Physics of Fluids*, Vol. 11, No. 5, May 2001, pp. 1067-1075.

[7]Andersson, P., Berggren, M., and Henningson, D.S., "Optimal Disturbances and Bypass Transition in boundary Layers," *Physics of Fluids*. Vol. 11, No. 1, Jan. 1999, pp. 134-150.

[8]Tumin, A. and Reshotko, E., "Spatial Theory of Optimal Disturbances in Boundary Layers," *Physics of Fluids*, Vol. 13, No. 7, Jul. 2001, pp. 2097-2104.

[9]Malik, M. R., "Stability Theory for Laminar Flow Control Design," *Viscous Drag Reduction in Boundary Layers*, AIAA, Washington, DC, 1990, pp. 3-41.

[10]Saric, W. S., Reed, H. L., and Kerschen, E. J., "Boundary-Layer Receptivity to Freestream Disturbances," *Annual Review of Fluid Mechanics*, Vol. 34, Jan. 2002, pp. 291-319.

[11]Tumin, A., "Multimode Decomposition of Spatially Growing Perturbations in a Two-Dimensional Boundary Layer," *Physics of Fluids*, Vol. 15, No. 9, Sep. 2003, pp. 2525-2540.

[12]White, E. B., Rice, J. M., and Ergin, F. G., "Receptivity of Stationary Transient Disturbances to Surface Roughness," *Physics of Fluids*, Vol. 17, No. 6, Jun. 2005, 064109.

[13]Denissen, N. A., Downs III, R. S., and White, E. B., "Transient Growth Due to Surface Roughness: Theory, Simulation and Experiment," AIAA Paper 2009-0175, Jan. 2009.

[14]Denissen, N. A. and White, E. B., "Continuous Spectrum Analysis of Roughness-Induced Transient Growth," *Physics of Fluids*, Vol. 21, No. 11, Nov. 2009, 114105.

[15]Ergin, F. G. and White, E. B., "Unsteady and Transitional Flows Behind Roughness Elements," *AIAA Journal*, Vol. 44, No. 11, Nov. 2006, pp. 2504-2514.

[16]Rizzetta, D. P. and Visbal, M. R., "Direct Numerical Simulations of Flow Past an Array of Distributed Roughness Elements," *AIAA Journal*, Vol. 45, No. 8, Aug. 2007, pp. 1967-1976.

[17]Stephani, K. A. and Goldstein, D. B., "DNS Study of Transient Disturbance Growth and Bypass Transition Due to Realistic Roughness," AIAA Paper 2009-0585, Jan. 2009.

[18]Simpson, R., "Junction Flows," *Annual Review of Fluid Mechanics*. Vol. 33, 2001, pp. 415-443.

[19]Bhattacharyya, S., Dennis, S. C. R., and Smith, F. T., "Separating Shear Flow Past a Surface-Mounted Blunt Obstacle," *Journal of Engineering Mathematics*, Vol. 39, Mar. 2001, pp. 47-62.

[20]Baker, C. J., "The Laminar Horseshoe Vortex," *Journal of Fluid Mechanics*, Vol. 95, Nov. 1979, pp. 347-367.

[21]Gregory, N. and Walker, W. S., "The Effect on Transition of Isolated Surface Excrescences in the Boundary Layer," Aeronautical Research Council, R&M 2779, 1956.

[22]Kim, J., Moin, P., and Moser, R., "Turbulence Statistics in Fully Developed Channel Flow at Low Reynolds Number," *Journal of Fluid Mechanics*, Vol. 177, Apr. 1987, pp. 133-166.

[23]Goldstein, D. B., Handler, R., and Sirovich, L., "Modeling a No-Slip Flow Boundary with an External Force Field," *Journal of Computational Physics*, Vol. 105, Apr. 1993, pp. 354-366.

[24]Goldstein, D. B., Handler, R., and Sirovich, L., "Direct Numerical Smulation of Trbulent Fow Over a Modeled Riblet Covered Surface," *Journal of Fluid Mechanics*, Vol. 302, Nov. 1995, pp. 333-376.

[25]Goldstein, D. B. and Tuan, T. C., "Secondary Flow Induced by Riblets," *Journal of Fluid Mechanics*, Vol. 363, May 1998, pp. 115-151.

[26]Colmenero, G. E., *Turbulent Boundary Layer Control with Discrete Actuators Using Wall Information*, Master's Thesis, The University of Texas at Austin, Dec. 2004.

[27]Moin, P. and Kim, J., "Numerical Investigation of Turbulent Channel Flow," *Journal of Fluid Mechanics*, Vol. 118, May 1982, pp. 341-377.

[28]Goldstein, D. B., Cohen, J., and Levinski, V., "DNS of Hairpin Vortex Formation in Poiseuille Flow Due to Two-Hole Suction," *Proceedings of the 3rd International Conference on DNS/LES*, Air Force Office of Scientific Research, Arlington, TX, Aug. 2001, pp. 501-508.

[29]White, F. M., "Laminar Boundary Layer," *Viscous Fluid Flow*, 3rd ed., McGraw Hill, New York, 2006, pp. 231-236.

[30]Strand, J. S., "DNS of Surface Textures to Control the Growth of Turbulent Spots," Master's Thesis, The University of Texas at Austin, Dec. 2007.

[31]Fischer, P. and Choudhari, M., "Numerical Simulation of Roughness-Induced Transient Growth ina Laminar Boundary Layer," AIAA Paper 2004-2539, Jun. 2004.

[32]Stephani, K. A., "Drag Reduction Using Trapped Bubbles on a Submerged Flat Plate Surface," Master's Thesis, The University of Texas at Austin, Dec. 2006.

[33]Dennissen, N. and White, E., "Roughness-Induced Bypass Transition, Revisited," *AIAA Journal*, Vol. 46, No. 7, Jul. 2008.

[34]Rice, J. M., "Roughness Receptivity and Scaling of Non-Optimal Transient Disturbances," Master's Thesis, Case Western Reserve University, Cleveland, OH.

[35]Tumin, A. and Reshotko, E., "The Problem of Boundary-Layer Flow Encountering a Three-Dimensional Hump Revisited," AIAA Paper, 2004-2539, 2004.

VITA

CJ Doolittle was born in Minneapolis, Minnesota on November 28th, 1985, to Chuck and Julie Doolittle. He grew up in Farmington, Minnesota after the age of seven where he stayed until graduating from Farmington Senior High School. After which, CJ attended the University of Minnesota until May of 2008 when he graduated Summa Cum Laude with Distinction in Aerospace Engineering and Mechanics. CJ continued his education at The University of Texas at Austin where his research efforts involve fluid dynamics under the direction of Dr. David Goldstein.

Permanent address: Residence of Chuck and Julie Doolittle

18853 Elite Ct.

Farmington, MN 55024

This thesis was typed by the author.